Spectral partitioning identifies individual heterogeneity in the functional network topography of ventral and anterior medial prefrontal cortex

Claudio Toro-Serey[1,2], Sean M. Tobyne[1,3], & Joseph T. McGuire[1,2]

1. Department of Psychological and Brain Sciences, Boston University, Boston, USA

2. Center for Systems Neuroscience, Boston University, Boston, USA

3. Graduate Program for Neuroscience, Boston University, Boston, USA

Corresponding authors: Claudio Toro-Serey (ctoro@bu.edu) & Joseph T. McGuire (jtmcg@bu.edu)

Highlights:

- The topography of Default Network cortical regions varies across individuals.

- A community detection algorithm, spectral partitioning, was applied to rs-fMRI data.

- The algorithm identified individualized Default Network regions in mPFC and PCC.

- Default Network topography varied across individuals in mPFC, moreso than in PCC.

- Overlap of task effects with DN regions should be assessed at the individual level.

1

Abstract

Regions of human medial prefrontal cortex (mPFC) and posterior cingulate cortex (PCC) are part of the default network (DN), and additionally are implicated in diverse cognitive functions ranging from autobiographical memory to subjective valuation. Our ability to interpret the apparent co-localization of task-related effects with DN-regions is constrained by a limited understanding of the individual-level heterogeneity in mPFC/PCC functional organization. Here we used cortical surface-based meta-analysis to identify a parcel in human PCC that was more strongly associated with the DN than with valuation effects. We then used resting-state fMRI data and a data-driven network analysis algorithm, spectral partitioning, to partition mPFC and PCC into "DN" and "non-DN" subdivisions in individual participants (n = 100 from the Human Connectome Project). The spectral partitioning algorithm identified individual-level cortical subdivisions that varied markedly across individuals, especially in mPFC, and were reliable across test/retest datasets. Our results point toward new strategies for assessing whether distinct cognitive functions engage common or distinct mPFC subregions at the individual level.

Keywords: functional connectivity, default network, network neuroscience, medial prefrontal cortex, spectral partitioning

2

1. Introduction

Human medial prefrontal cortex (mPFC) and posterior cingulate cortex (PCC) are jointly associated with a diverse set of cognitive processes (Hiser & Koenigs, 2018; Kragel et al., 2018), and contain subregions that are part of the brain's default network (Buckner & DiNicola, 2019; DN; Buckner et al., 2008). DN regions are characterized by a decrease in BOLD activity during externally oriented tasks that require attention or cognitive control, in comparison with less-demanding task conditions or periods of rest (Buckner et al., 2008; Laird et al., 2009; McKiernan et al., 2003). The DN can also be identified on the basis of a distinctive pattern of inter-region correlations in resting-state fMRI data (Buckner et al., 2008; Fox et al., 2005; Greicius et al., 2003; Yeo et al., 2011).

Many different cognitive task manipulations evoke patterns of brain activity that overlap with DN regions in ventral and anterior mPFC and in PCC. Examples include manipulations of self-referential thinking (Gusnard et al., 2001; Mitchell et al., 2005), memory (Euston et al., 2012; Schacter et al., 2007), affective regulation (Reddan et al., 2018; Schiller et al., 2008), and subjective valuation (Bartra et al., 2013; Clithero & Rangel, 2014; Kable & Glimcher, 2007; Levy et al., 2011). Some of these task-related effects are thought to reflect processes integral to the functional role of the DN, such as internally oriented cognition, scene construction, and self-projection (Buckner & Carroll, 2007; Hassabis & Maguire, 2007). For other task-related effects, such as subjective valuation (i.e., greater BOLD activity in response to more highly valued choice prospects and outcomes, relative to prospects and outcomes that are less highly valued), the degree of overlap with DN regions is only partial and the reason for the overlap is less obvious (Acikalin et al., 2017). Insofar as the DN shares a subset of nodes in common with the distributed brain systems that support valuation and other functions, this has potential to inform our theoretical understanding of the cognitive operations involved in those functions (Northoff & Hayes, 2011). As a result, there is widespread interest in understanding the degree to which DN regions overlap topographically with task-related effects (Buckner & DiNicola, 2019; DiNicola et al., 2019; Spreng, 2012).

However, strong conclusions about functional colocalization require consideration of individual-level heterogeneity in topographic patterns of brain activity. A recognized limitation of group averaging and meta-analysis is that the functional topography of individual brains can be misaligned and blurred (Fedorenko et al., 2012; Guntupalli et al., 2018; Michalka et al., 2015; Tobyne et al., 2018; Wang et al., 2015; Woo et al., 2014), exaggerating the apparent overlap across domains. This concern is especially pronounced in ventral mPFC, which is subject to considerable idiosyncratic cortical folding (Lopez-Persem et al., 2019; Mackey & Petrides, 2014; Zilles et al., 2013) and inter-subject functional variability (Mueller et al., 2013). An alternative

61 approach is to focus on analyses at the individual-participant level. Individual-level analyses of fMRI data

62 have identified idiosyncratic, reliable, and valid patterns of functional organization that would be blurred

63 in aggregative estimates (Gordon et al., 2017; Gratton et al., 2018; Laumann et al., 2015; Michalka et al.,

64 2015; Tobyne et al., 2018), and subject-specific network arrangements have been found to predict behavioral

65 characteristics (Kong et al., 2018). Recent work has uncovered fine-grained subdivisions within the DN using

66 both data-driven clustering and individually customized seed-based connectivity analysis (Braga & Buckner,

67 2017; Braga et al., 2019). It is therefore possible that the apparent overlap of the DN with task-related effects

68 might, in some cases, be attributable to low effective spatial resolution, and that the organization of mPFC

69 and PCC might be better understood at the individual level. An important first step in investigating this

70 possibility, and the goal of the present paper, is to quantify the degree of variability in the topography of the

71 DN within mPFC and PCC across a large sample of individuals.

72 A useful way to characterize individual-specific brain organization is to examine patterns of resting-state

73 functional connectivity. Connectome-based analyses of resting-state functional connectivity have been fruitful

74 in identifying individualized functional subregions that correspond well to task-induced activity patterns

75 (Gordon et al., 2017; Laumann et al., 2015; Smith et al., 2009; Tobyne et al., 2018). A functional connectome

76 can be represented in the form of a network, and graph theoretic methods can be applied to analyze the

77 network's structure (Bassett & Sporns, 2017; Rubinov & Sporns, 2010). In the context of network analysis,

78 community detection algorithms subdivide brain networks into sets of nodes that share more connections

79 with each other than with the rest of the network (Fortunato & Hric, 2016; Garcia et al., 2018). Here we use

80 the technique of spectral partitioning (SP), an efficient community detection algorithm that deterministically

81 subdivides a network into two communities (Belkin & Niyogi, 2003; Chung, 1997; Fiedler, 1975). SP has

82 previously been used to characterize the posterior-anterior functional gradient of the insula using resting-state

83 fMRI data (Tian & Zalesky, 2018), and was shown to robustly and reliably separate both simulated and

84 actual primate ECoG networks (Toker & Sommer, 2019). We use SP here to identify subsets of nodes within

85 mPFC and PCC that share spontaneously covarying temporal activation patterns during rest.

86 In this study, we aimed to subdivide mPFC and PCC into individual-specific DN and non-DN communities,

87 and to quantify the degree of topographic heterogeneity in the resulting community structure over time and

88 across individuals. We did this by capitalizing on the respective strengths of meta-analysis and subject-specific

89 analyses of brain networks. We used a data-driven network-analysis procedure to identify two communities

90 that each spanned both mPFC and PCC in each individual participant. We found that the resulting

91 communities had a stereotyped topographic layout within PCC (according to a label-agnostic similarity

92 metric), whereas their layout in mPFC was variable across individuals but stable across test/re-test. We

4

93 took advantage of the more consistent configuration within PCC to assign meta-analysis-derived labels to the

94 two communities. Because our data-driven method established correspondence between PCC subregions and

95 mPFC subregions, the labels defined in PCC could then be indexed into the more heterogeneous community

96 structure of mPFC in each individual.

97 The outline of our paper is as follows. First, we defined a search space by selecting parcels from an established

98 brain atlas (Glasser et al., 2016) that corresponded to previously defined DN and limbic networks on the

99 medial cortical wall (Yeo et al., 2011). A cortical surface-based meta-analysis of the DN and valuation

100 literatures identified a parcel in PCC that was DN-specific at the aggregate level. Valuation was selected as an

101 example of a cognitive domain in which group-average activity patterns overlap extensively with DN regions

102 on the medial surface, despite being segregable elsewhere (Acikalin et al., 2017). We then derived a functional

103 connectivity network of all the surface vertices within the search space for each of 100 individual resting-state

104 fMRI data sets from the Human Connectome Project (HCP; Van Essen et al., 2012), and used the SP

105 algorithm to subdivide each individual's network into DN and non-DN communities (labeled according to

106 which community included the meta-analytically identified DN-specific parcel in PCC). Focusing on individual

107 vertices in the search space rather than the parcels (as is typical in brain network analyses) allowed us to

108 finely delineate the topographic extent of each community. The resulting communities varied topographically

109 across individuals, while also appearing to follow common organizational principles. Test-retest analyses

110 showed that these partitionings were similar across scanning days within (but not between) individuals,

111 and that individual-level idiosyncrasy was greater in mPFC. Partitionings obtained from the SP algorithm

112 had higher test-retest reliability than did analogous results from seed-based functional connectivity. We

113 observed a trend for the DN community to be located within principal sulci in ventral mPFC and left PCC,

114 but in gyri within superior mPFC and right PCC. Lastly, we describe how the structure of the resulting

115 automatically defined DN and non-DN communities both aligns with and differs from a recently proposed

116 scheme for identifying subdivisions within the DN (Braga & Buckner, 2017; Braga et al., 2019). Our work

117 highlights the usefulness of estimating brain effects at the individual level in mPFC and PCC, and provides a

118 new framework and tool set for future investigations of overlap across cognitive domains.

2. Material and Methods

2.1. *Data and Code Accessibility Statement*

121 All code used in this study is openly available at https://github.com/ctoroserey/mPFC_partitioning. Resting-

122 state fMRI data were obtained from the Human Connectome Project (Van Essen et al., 2012).

5

2.2. *Search space*

For all analyses, we defined our search space based on the 17-network parcellation proposed by Yeo et al. (2011). First, we selected vertices on the medial cortical surface that were contained by the DN and limbic networks in HCP's 32,000 vertex surface space (fs_LR_32k). Next, we overlaid those networks on a parcellated atlas of the human cortical surface (360 regions; Glasser et al., 2016), and retained a set of parcels that covered approximately the same brain regions (visually inspected, retaining parcels that appeared to have at least 15% overlap). This resulted in a search space that consisted of 40 parcels across hemispheres (Supplementary Table 1). The search space in each hemisphere was naturally divided into two spatially non-contiguous clusters in PCC and mPFC, facilitating the examination of each region separately.

2.3. *Meta-analysis*

We used a novel approach to cortical surface parcel-based meta-analysis to assess whether individual parcels within the search space were preferentially associated with subjective valuation or with decreased activity during externally oriented tasks, which served to operationalize the DN. For subjective valuation, we gathered peak activation coordinates from 200 studies that reported positive effects in contrasts of higher-value minus lower-value outcomes or prospects (Bartra et al., 2013). For the DN, we acquired coordinates from 80 studies that reported reductions in BOLD during externally directed tasks compared to a baseline (Laird et al., 2009). The coordinates represent areas that exceeded the statistical significance threshold in each original study. For each study, we created an indicator map in standard volumetric space (MNI152, 1 mm resolution) which contained values of 1 in a 10 mm radius sphere around each reported activation peak, and values of 0 elsewhere (Wager et al., 2009). The indicator map for each study was then projected to a standard cortical mesh (fsaverage, 160,000 vertices, projfrac-max from 0 to 1 by 0.25, registered using mni152.register.dat) using FreeSurfer's mri_vol2surf (Dale et al., 1999; Fischl et al., 1999) (http://surfer.nmr.mgh.harvard.edu/). We then resampled the Glasser et al. (2016) parcellation to fsaverage, and tallied how many studies had positive indicator values intersecting with each cortical parcel (the details of the resampling procedure are described in https://wiki.humanconnectome.org/display/PublicData/HCP+ Users+FAQ#HCPUsersFAQ-9.HowdoImapdatabetweenFreeSurferandHCP, and were implemented using a custom script available at https://github.com/stobyne/Spherical-Surface-Swapper). Two studies from the subjective valuation corpus were removed because they did not contain activation peaks that overlapped with cortex, leaving a final number of 198 studies.

To test for parcels that were significantly more strongly associated with one domain than the other, we

153 performed per-parcel chi-squared tests comparing the proportion of studies with activation in that parcel

154 between the two domains. We permuted the study domain labels (DN or valuation) 5000 times while

155 preserving the total number of studies in each domain, and on each iteration stored the maximum resulting

156 chi-squared statistic across all parcels. This gave us a null distribution of 5000 maximum chi-squared

157 values. The 95th percentile of this distribution served as an FWE-corrected significance threshold to evaluate

158 unpermuted chi-squared values.

159 **2.4. *Resting-state fMRI Data***

160 Our fMRI analyses used resting-state fMRI data from the Human Connectome Project (Van Essen et al.,

161 2012) Q6 release (N = 100, randomly sampled from the total pool of 469 available subjects). The Washington

162 University Institutional Review Board approved all experimental procedures, and all subjects provided written

163 informed consent in accordance with the guidelines set by the institution. Each subject's data was acquired

164 over two days at Washington University in St. Louis on a Siemens CONNECTOM Skyra MRI scanner

165 (Siemens, Erlangen, Germany). Four resting state runs (repetition time = 0.720 s, echo time = 33.1 ms, flip

166 angle = 52°, multiband factor = 8, 72 slices, 2 mm isotropic voxels) each comprised 1200 time points (14 min

167 24 s) for a total of 4800 time points. Two runs were acquired on each day, with the phase encoding direction

168 set to left-right for one run and right-left for the other. Only subjects with both left-right and right-left

169 phase encoding for each day were included (i.e. subjects with four resting-state fMRI sessions). In addition,

170 only datasets with low motion levels (under 1.5 mm) and less than 5% of points over 0.5 mm framewise

171 displacement (FD; Power et al., 2014) were used. See (Van Essen et al., 2012) for more details about the

172 data acquisition protocol.

173 Data initially underwent the HCP minimal preprocessing pipeline (Glasser et al., 2013), which included

174 gradient nonlinearity correction, motion correction, EPI distortion correction, high-pass filtering (0.0005

175 Hz threshold), MNI152-based normalization, surface reconstruction, and mapping of functional data to a

176 standardized cortical surface model (details can be found in Glasser et al., 2013). In addition, data underwent

177 temporal denoising based on independent components (FMRIB's ICA-based X-noiseifier, FIX; Griffanti et al.,

178 2014; Salimi-Khorshidi et al., 2014). Data were further preprocessed using an in-house pipeline described

179 previously (Tobyne et al., 2017). Steps (in order) included linear interpolation across high motion timepoints

180 with over 0.5 mm of FD, band-pass filtering (allowed frequencies ranged from 0.009 and 0.08 Hz), and

181 temporal denoising via mean grayordinate signal regression (Burgess et al., 2016). Interpolation of high

182 motion time points was performed to avoid temporal smoothing of noisy signal from head motion into the

183 filtered signal during the bandpass procedure. After filtering and denoising, the interpolated high-motion

7

184 time points were censored by deletion and each run was temporally de-meaned. The processed time series

185 had a median of 4799 time points (minimum = 4661) across participants. Each subject's brain was comprised

186 of 32k standard grayordinates per hemisphere (combined in a CIFTI file). We retained only the cortical

187 surfaces, which resulted in 59,412 total surface vertices per subject.

188 **2.5. *Network Definition***

189 All network analyses were performed using the igraph package (v. 1.1.2; https://igraph.org/r/; Csardi &

190 Nepusz, 2006) in R (v. 3.4.1; https://www.r-project.org/; R Core Computing Team, 2017). To establish

191 each subject's network, we selected all the vertices contained within the mPFC/PCC search space (n =

192 4,801 per subject; mPFC = 2854, PCC = 1947) and computed the Pearson correlation of the time series

193 for every pair of vertices. All correlation values were transformed using Fisher's r to z. This produced a

194 weighted network for each subject, in which the nodes were surface vertices and the edge weights were the

195 correlations among them. Edges mostly consisted of positive correlations (mean proportion positive = 0.65,

196 SD = 0.03). We chose not to threshold the network, as the SP algorithm is well equipped to operate on

197 complete (i.e. fully-connected) weighted graphs (Chung, 1997). However, our results were unchanged if we

198 retained only significant correlations ($p < 0.05$, uncorrected) in the weight matrices. Next, we took the

199 exponential of the z-transformed correlations so that all weights became positive while maintaining their

200 ordinal ranks. Ensuring that all edges were positive facilitated the construction of the graph Laplacian (see

201 below), which requires all off-diagonal elements to have the same sign by design. We generated and analyzed

202 network weight matrices at four levels: (1) for each subject's full concatenated dataset (up to 4800 TRs); (2)

203 on each step of a sliding window analysis (see Section 2.7 for more details); (3) for the concatenated time

204 series for the two runs on each day (up to 2400 TRs); and (4) for each run separately (up to 1200 TRs).

205 **2.6. *Community Detection***

206 Communities (i.e. clusters) were identified using the SP algorithm (Belkin & Niyogi, 2003; Chung, 1997;

207 Fiedler, 1975; Higham et al., 2007). First, each network was represented as an n x n network weight matrix

208 W as described above (where n equals the number of vertices in the search space, 4,801). The matrix was

209 then transformed into its symmetric normalized Laplacian form

$$L = I - D^{-\frac{1}{2}} W D^{-\frac{1}{2}}$$

8

210   where I is an identity matrix of size n, and D is a diagonal matrix containing the strength of each vertex

211   (i.e. the sum of its edge weights with all other vertices). This resulted in a matrix wherein each entry was the

212   negative normalized value of the connection (from 0 to 1) between any two vertices relative to their combined

213   connectivity strength, and with ones along the diagonal. The transformation ensures that every row sums to

214   zero. We then computed the eigenvalues and eigenvectors of the symmetric normalized Laplacian matrix,

215   and used the eigenvector associated with the second-to-lowest eigenvalue (traditionally called the 'Fiedler

216   vector') to divide the network into two. The Fiedler vector consists of a set of positive and negative values

217   and is binarized by sign to partition the network into two similar-sized communities (Fiedler, 1975). In this

218   way, SP avoids producing communities that are too small to be physiologically meaningful (for example,

219   small sets of vertices that are spuriously correlated due to measurement noise). Given that this data-driven

220   method does not label the two communities or establish correspondence across participants, we defined each

221   individual's "DN" community as that which contained the majority of the vertices in the DN-specific PCC

222   parcel identified in our meta-analysis (area 7m). The completeness of the graphs ensured that SP did not

223   face the issues associated with its use in sparse networks (Fortunato & Hric, 2016).

224   In order to evaluate the validity of the resulting partitionings across community-detection methods, we also

225   estimated network communities using the more traditional approach of modularity maximization (Garcia et

226   al., 2018), based on the algorithm from Clauset et al. (2004). The method heuristically iterates through

227   many possible combinations of vertices, and selects the partitioning that maximizes the within-community

228   edge weights, relative to a random network containing the same number of edges and communities. Unlike SP,

229   modularity can fractionate a network into more than two communities. Agreement between the partitions

230   provided by the bounded (SP) and unbounded (modularity) community detection methods would suggest the

231   results are not distorted by the restriction of SP to binary partitionings.

232   **2.7.** *Partition Evaluation*

233   We used the Adjusted Rand index (ARI) to evaluate the stability and topographical heterogeneity of the

234   communities within and across individuals (Hubert & Arabie, 1985), which was calculated using the "mcclust"

235   package in R (Fritsch, 2012). The ARI is a metric that quantifies the similarity between two alternative

236   clusterings of the same data. The base of the ARI is computed by the formula

$$\frac{a+b}{a+b+c+d}$$

237   where a is the number of pairs of nodes that were grouped together in both partitionings, b is the number

9

238 that were grouped separately, and c and d denote the number of pairs grouped together (separately) in one

239 partitioning, but separately (together) in the other. Therefore, the ARI estimates the fraction of all possible

240 node pairs that had the same status (connected or not) in both partitionings (with the denominator equal to

241 $n(n-1)/2$). The resulting ratio is adjusted against a baseline given by the expectation assuming independent

242 partitionings to yield an index that ranges from 0 to 1, where 0 denotes the value expected by chance. This

243 means that even though differences are heavily penalized, positive ARI values compare favorably against

244 chance clustering (and the index can take negative values if the ratio given by the formula above falls below

245 the chance level). In short, the ARI quantifies the chance-corrected agreement between any two partitions

246 while being agnostic to the labeling scheme.

247 We performed a number of comparisons among partitions. First, we computed the degree of agreement

248 between SP and modularity maximization per subject. SP and modularity maximization have been previously

249 found to show a tendency toward underfitting and overfitting, respectively, in their community detection

250 performance in a diverse set of network types (Ghasemian et al., 2019), so alignment between the two

251 algorithms would increase our confidence in the validity of the resulting partitionings. Next, we compared

252 the subject-level SP partitionings across individuals, and calculated the mean pairwise ARI for the group.

253 We then performed the same evaluation for PCC and mPFC separately, and examined whether there were

254 differences in overall agreement within these regions by performing a paired permutation analysis. For each

255 individual and region we took the mean ARI with all 99 other individuals, then took the difference between

256 regions to get an ARI difference per subject. On each of 5000 permutations each subject's ARI difference was

257 independently sign-flipped and the group mean difference was added to a null distribution. The unpermuted

258 group mean difference was then evaluated against this permuted distribution.

259 To identify vertices whose community assignment was more stable or more variable, we performed a sliding

260 window analysis (20 min windows, 1 min increments, median number of windows per subject = 37, range =

261 35 - 37), comparing each window's resulting partitioning against the partitioning derived from the subject's

262 whole data set. A 20-min window has previously been found to yield relatively stable and unbiased estimates

263 of individual-level brain network characteristics (Gordon et al., 2017). We assessed whether the magnitude of

264 the Fiedler vector value for a given vertex (for the full subject-level data set) was associated with the stability

265 of that vertex's sub-network assignment across time windows. To do this, we fit a mixed effects logistic

266 regression model, in which the dependent variable was the proportion of times each vertex participated in the

267 DN community across windows, and the explanatory variables included a random effect of subject and a

268 fixed effect of the Fiedler vector value for that vertex (derived from their full time series). Based on this

269 significant relationship, we identified a threshold Fiedler vector value for each subject, such that empirical

10

²⁷⁰ above-threshold vertices were persistently associated with either DN or non-DN more than 99% of the time.

²⁷¹ We then estimated the level of agreement between network partitions estimated using data across individual
²⁷² scan days (with 2 days per participant). If the functional organization estimated by SP is indeed individual-
²⁷³ specific, we should see higher agreement within individual (test/re-test across days) than across individuals.
²⁷⁴ We tested this idea by computing the ratio of the mean ARI within and between individuals. Ratios close to
²⁷⁵ one would denote similar within-participant and across-participant alignment, whereas ratios considerably
²⁷⁶ higher than one would suggest that partitions were more similar within-participant than across participants.
²⁷⁷ We then extended this idea by computing the agreement across individual runs (4 per subject). Similar to
²⁷⁸ the day-based analysis, we assessed whether run-level data showed higher agreement within-subject than
²⁷⁹ between subjects.

²⁸⁰ **2.8. *Seed-based Resting-state Functional Connectivity versus Community Detection***

²⁸¹ We evaluated the performance of the SP algorithm in comparison to a simpler partitioning approach based
²⁸² on seed-based functional connectivity. Independently for each day (2 per individual), we estimated each
²⁸³ subject's DN partition in mPFC based on its vertex-wise functional correlations (Pearson) with the spatially
²⁸⁴ averaged activity across all vertices in the PCC search space. We used the whole PCC region because it is
²⁸⁵ traditionally thought to be a prominent node of the DN (Buckner et al., 2008), and is a common area for
²⁸⁶ researchers to place seeds for vertex- and volume-based connectivity analyses (e.g. Fox et al., 2005). We
²⁸⁷ compared these seed-based maps with the unthresholded Fiedler vectors produced by SP, with the sign of the
²⁸⁸ Fiedler vector oriented so the DN community was marked by positive values in every subject. We calculated
²⁸⁹ three sets of across-day similarity values for each individual: 1) between the two seed-based maps; 2) between
²⁹⁰ the two SP-based maps; and 3) between seed- and SP-based maps. Because the values in the maps were
²⁹¹ continuous-valued (and not categorical labels, which would be amenable to ARI), we quantified the similarity
²⁹² between maps in terms of the spatial Spearman correlation across vertices. These spatial correlations were
²⁹³ meant to determine the test/re-test reliability of each approach, as well as the overall level of agreement
²⁹⁴ between them. For 8 subjects, the communities produced with one of the days' data sets had split coverage
²⁹⁵ of area 7m, and our community labeling scheme for the Fiedler vector produced a sign mismatch across
²⁹⁶ days. ARI is robust to such labeling issues, but the inconsistency produced strong negative correlations of
²⁹⁷ the Fiedler vector across days for these individuals. Visual inspection showed that the community layout
²⁹⁸ was well aligned across days, and so we matched the labeling of their partitionings based on the day that
²⁹⁹ sufficiently covered area 7m.

11

The two methods were expected to produce somewhat similar results, but the one displaying greater within-subject agreement across days should be preferred (for a discussion on the stability of functional networks see Kong et al. (2018) and Gratton et al. (2018)). We therefore compared the within-subject spatial correlation coefficients produced by each method through a paired permutation analysis. For each of the 100 individuals, we computed the difference in inter-day correlations between methods, randomized the sign of these values 5000 times, and computed the mean of these differences on each iteration. The empirical difference in means was then evaluated against this permuted distribution.

2.9. *Associations with sulcal morphology*

Next we asked whether the location of the DN and non-DN communities was systematically related to sulcal morphology. Based on a previous report of individual alignment of DN within sulci in ventral mPFC (vmPFC; Lopez-Persem et al., 2019), we subdivided our search space into three regions: vmPFC, which matched the ROI used by Lopez-Persem and colleagues (2019; areas 25, s32, a24, 10v, 10r, p32, and OFC); superior mPFC (sup-mPFC), encompassing the remaining dorsal areas in our mPFC space; and all of the PCC search space. We used each subject's curvature maps from the HCP (transformed to fs_LR 32k space), in which cortical depth is quantified by negative numbers for sulci and positive numbers for gyri. For each individual, we computed the Spearman correlation between curvature and the unthresholded Fiedler vector values in each region and hemisphere separately (6 correlations per individual). Since the DN was indicated by positive FV values, negative correlations meant that the DN was more likely to be contained in sulci, with non-DN located in gyri. Finally, we collected all individual correlations for each combination of hemisphere and region, and performed a one-sample t-test on each set to determine whether correlations were significantly different from 0 in our group (6 tests total).

3. Results

3.1. *Meta-analysis*

We performed a coordinate-based meta-analysis to identify cortical surface parcels within mPFC and PCC that were preferentially associated with the DN or with subjective valuation. Volumetric coordinates from 80 studies with task deactivation contrasts and 198 studies with valuation contrasts were projected onto a cortical surface, and mapped to discrete parcels from a multimodal cortical parcellation (Glasser et al., 2016) to produce a list of brain areas reported per study. The 40 parcels considered were limited to the

12

328 medial portion of the default and limbic networks defined by the Yeo et al. (2011) 17-network parcellation.

329 Domain-specificity was tested by first permuting the domain labels across studies (DN or valuation) to create

330 a null distribution for the maximum chi-squared statistic in the search space (see Methods for details). The

331 null distribution was used to identify regions that were reported significantly more often in one literature or

332 the other.

333 Figure 1 shows the proportion of times each parcel was reported for each domain, as well as the significant

334 differences between domains. The 95th percentile of the permuted chi-squared distribution was 8.87. Based

335 on this threshold, area 7m in PCC/precuneus was the only parcel to show a preferential association with

336 the DN bilaterally (Left: observed $\chi^2 = 10.07$, $p = 0.029$; Right: observed $\chi^2 = 18.89$, $p < 0.001$). The

337 adjacent area v23 exhibited a similar effect, albeit only unilaterally (Right: observed $\chi^2 = 11.51$, $p = 0.011$;

338 Left: observed $\chi^2 = 8.25$, $p = 0.067$). There appeared to be a bilateral preference toward valuation effects

339 in mPFC area 25 (Left: observed $\chi^2 = 12.91$, $p = 0.005$; Right: observed $\chi^2 = 12.83$, $p = 0.005$); however,

340 closer inspection suggested this effect was driven by subcortical foci centered in adjacent ventral striatum. No

341 other parcels were preferentially implicated in valuation relative to DN. We therefore selected area 7m as an

342 interpretable, bilateral reference point for labeling DN and non-DN communities in the analyses that follow.

343 We note that the area labeled 7m in the parcellation used here (Glasser et al., 2016) is different from (and

344 located inferiorly on the medial surface to) the non-DN area 7m discussed in previous work (Andrews-Hanna
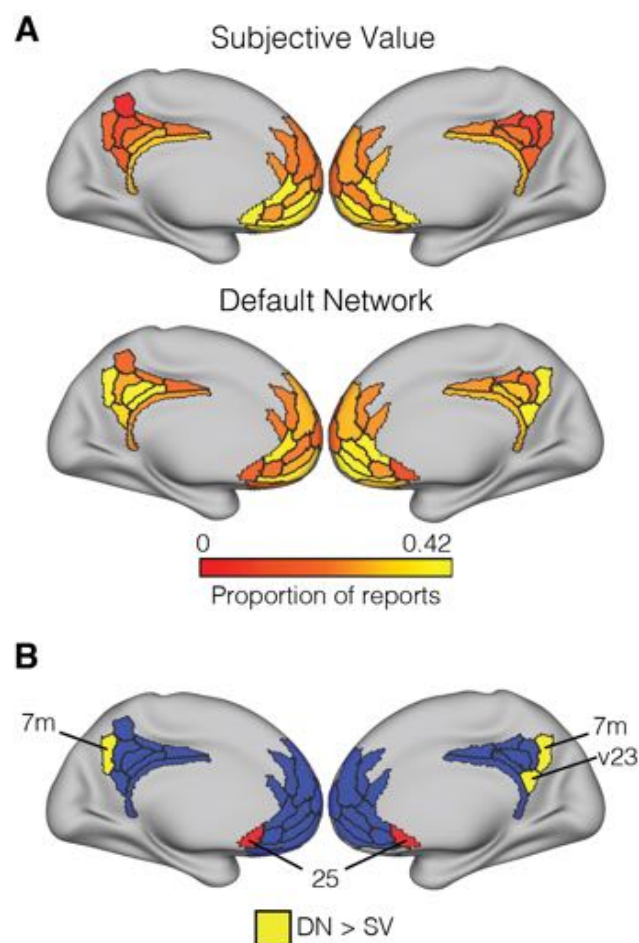
345 et al., 2010).

13

Figure 1: Figure 1. Meta-analysis results. A: Proportion of times each ROI was reported in the valuation and DN literatures. B: Regions identified in permutation-based chi-squared tests contrasting the two literatures. Area 25 (in red) initially appeared to be associated with valuation, but was not interpreted because the effect was found to reflect carryover from subcortical foci centered in ventral striatum (see text for details). Areas in blue represent the remainder of the search space.

3.2. *Individual-level DN and non-DN communities*

Within the mPFC/PCC search space, we estimated the topography of the DN for each individual. Using each individual's full time series (approximately 4800 total TRs from four 14-min scanning runs acquired over two days), we calculated the full vertex-to-vertex correlation matrix for the 4801 surface vertices in the search space. We represented each individual's correlation matrix in the form of a network, with cortical surface vertices as nodes and transformed correlation values as edge weights. We then applied the SP community detection algorithm to partition the network into two cohesive functional communities.

14

353 Figure 2 shows a representative partitioning of the search space for a single participant (100307; additional

354 examples are presented in the first two columns of Supplemental Figure 1). The SP algorithm subdivides

355 a network according to the positive versus negative values in the Fiedler vector (the eigenvector related to

356 the second-to-lowest eigenvalue of the network's normalized Laplacian matrix, see Methods). Since this is a

357 data-driven approach, there is no a priori labeling for the two communities. We assigned the DN label to the

358 community that contained the majority of the DN-specific PCC parcel from the meta-analysis (7m). We

359 oriented each individual's Fiedler vector so positive values corresponded to the DN community (Nenning

360 et al., 2017), and were assigned a value of 1 in the binarized partitionings (with 0 denoting non-DN). In

361 qualitative terms, the resulting patterns contained substantial DN coverage in posterior PCC (as dictated

362 by our labeling strategy), with non-DN vertices in anterior PCC. The mPFC region tended to include DN

363 vertices in its ventral-anterior and dorsal-anterior areas, with a persistent non-DN pocket between them. This

364 non-DN section extended posteriorly into pregenual cingulate cortex (area a24). We note that the addition of

365 restrosplenial cortex (an area commonly regarded as part of canonical DN) to the search space did not change

366 these results; as expected, that area tended to be largely assigned to the DN community (Supplemental
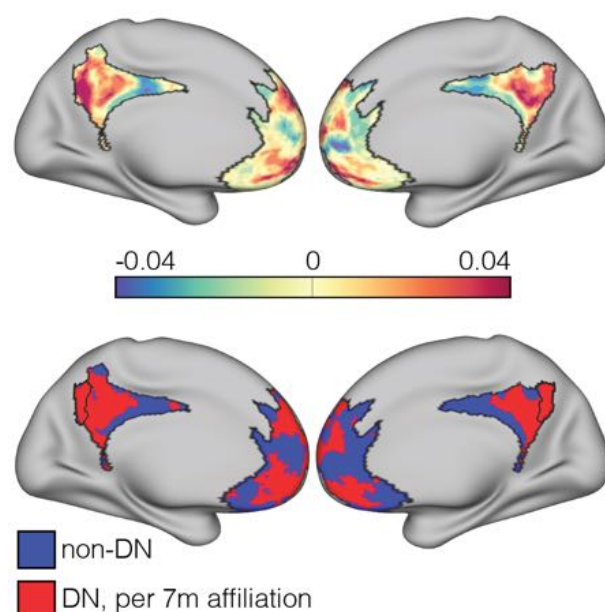
367 Figure 1).

15

Figure 2: Figure 2. Brain partition for an example subject (100307). Fiedler vector values (top) are mapped onto the brain surface, dividing it into positive and negative communities. The bottom brain shows the binarized Fiedler vector, with red areas denoting the DN community (as indicated by coverage of area 7m, bordered).

Before evaluating the degree of generalizibility of this topographic pattern across individuals, we examined the validity of the partitionings by comparing them to results from an alternative community detection algorithm, modularity maximization (Clauset et al., 2004). Modularity seeks to find the set of communities that maximizes within-community connection weights relative to a null model. Since modularity is not constrained to a predetermined number of communities, it was capable of finding more than two in our data set. We quantified the cross-method agreement in terms of the Adjusted Rand Index (ARI; see Methods), which measures the proportion of node pairs in a network that were either clustered together or separately in both partitionings, while being agnostic to labeling schemes and controlling for chance clustering. The ARI normally takes values ranging from 0 to 1, with 0 indicating chance agreement (but can take negative values if the similarity falls below chance). Supplemental Figure 2 contains examples of ARI values in real and simulated contexts.

The two clustering methods had high agreement (mean ARI = 0.87, SD = 0.13). Modularity showed a tendency to produce additional communities (median = 3, range = 2, 5). However, the additional communities

16

381 encompassed a small number of vertices (median = 16.5, IQR = 6 - 41.5) compared to the principal two

382 (median = 4783.5, IQR = 4759.5 - 4795), suggesting that a binary partitioning provided a reasonable

383 approximation of the network's true community structure.

384 Next, we examined the similarity of SP-based partitionings across individuals by computing the ARI between

385 every pair of subjects, and found modestly above-chance agreement overall (mean = 0.13, SD = 0.05).

386 Qualitative inspection of the community organization showed good alignment for PCC, whereas the pattern

387 in mPFC was consistent but shifted topographically across subjects. To quantify this heterogeneity in mPFC,

388 we calculated the between-subject ARI for each region separately (Figure 3). The functional topography

389 of PCC was better aligned across individuals (mean = 0.19, SD = 0.09) than mPFC (mean = 0.1, SD =

390 0.05; paired permutation, $p < 0.001$; Cohen's D = 1.26), although the mean ARI in mPFC still exceeded the

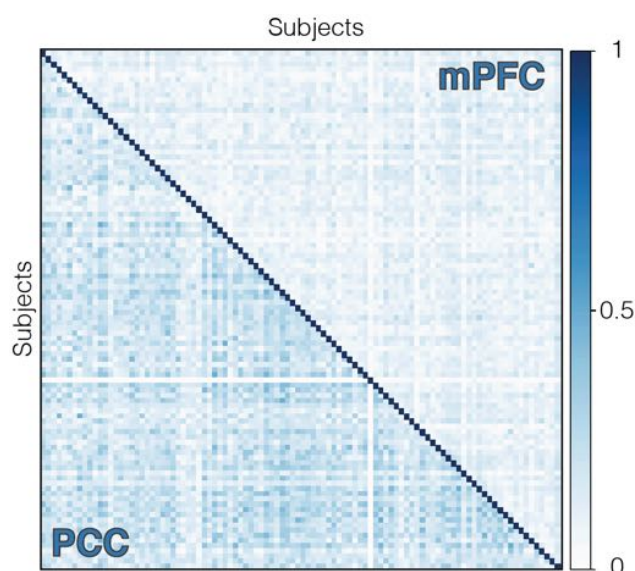391 chance value of zero (Wilcoxon signed rank test, $p < 0.001$; Cohen's D = 2.03).

Figure 3: Figure 3. Similarity matrix showing ARI values among all subjects for PCC (lower triangle) and mPFC (upper triangle) separately. Functional topographic patterns were better aligned across individuals in PCC than mPFC.

392 **3.3. *Pattern variability over time***

393 We next sought to estimate whether individual vertices had a stable or unstable community affiliation over

394 time. We did so by performing a sliding window analysis on each subject's full time series (20 min windows

395 shifting by 1 min). We compared the partitioning derived from each window with the partitioning computed

396 using the entire time series (Figure 4). Our focus here was not on the overall level of agreement (which is

17

397 expected to be high given the use of overlapping data), but on differences in stability across nodes. The

398 sliding window analysis provided a means to identify nodes that were highly variable, and allowed us to

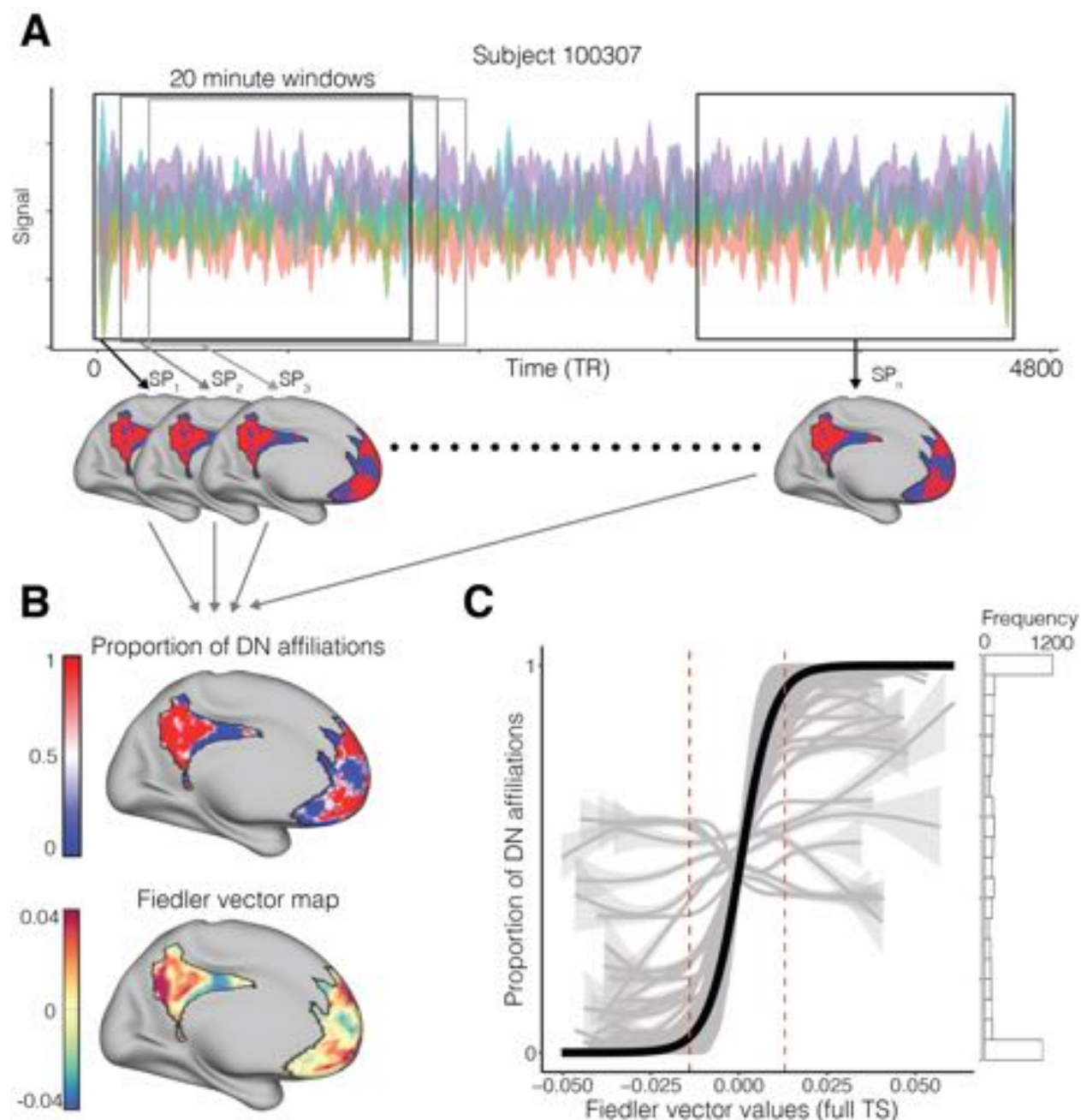399 determine whether these variable nodes followed a specific spatial structure.

18

Figure 4: Figure 4. A: For each individual, we produced partitions for each 20 minute sliding window (84 TRs). B: Proportion of times each vertex was affiliated with the DN community across windows in one example subject (upper), and the continuous Fiedler vector map for the same subject using their full time series (lower). C: Relationship between the magnitude of Fiedler vector values and the proportion of DN affiliations. Grey lines display data for each subject, and the black line shows the fit from a mixed-effects logistic regression. Dashed red lines indicate the mean FV value at which maps were thresholded. The histogram displays the mean frequency distribution of y-axis values.

400 The mean ARI along each subject's time series was significantly higher for PCC (mean = 0.59; SD = 0.14)

401 than mPFC (mean = 0.5; SD = 0.13; paired permutation, $p < 0.001$; Cohen's D = 0.65). A subset of nodes

402 showed exceptionally high stability, in that they were assigned to the same community in every time window.

403 The percentage of stable nodes ranged from 0 to 73% across individuals (median = 49.5%, IQR = 29% -

404 60.25%).

405 We next tested whether the continuous-valued Fiedler vector (before binarization into discrete communities)

406 carried information about the stability of individual nodes. There is precedent in the literature for the

407 idea that the magnitude (and not just the sign) of the Fiedler vector values conveys important information

408 about the role of each node in the network (Gkantsidis et al., 2003; Tian & Zalesky, 2018). Therefore, we

409 tested whether the magnitude of the eigenvector values was associated with the stability of nodes over time.

410 Specifically, we estimated the proportion of DN affiliations per node as a function of Fiedler vector values,

411 using a logistic mixed effects model (Figure 4). The model identified a positive significant relationship between

412 these features ($\beta = 217.02$, SE = 0.67, $p < 0.001$), signifying that vertices with higher absolute Fiedler vector

413 values were more persistent in their relationship with their corresponding community over time.

414 These analyses suggest that there is potential value in thresholding the Fiedler vector as a means to identify

415 reliable DN and non-DN vertices on an individual subject basis. We therefore thresholded each subject's

416 Fiedler vector to produce these refined maps. For each individual, we estimated the threshold by selecting

417 the empirical smallest absolute Fiedler vector value that yielded an average stability across suprathreshold

418 nodes of 99%, for positive (mean = 0.0132, SD = 0.006) and negative (mean = -0.0139, SD = 0.0069) values

419 separately. Individuals without such stable nodes (n = 19) were not thresholded, and were included in the

420 subsequent analyses in unthresholded form. The median proportion of retained vertices per individual was

421 0.49 (IQR = 0.29 - 0.65). Sub-threshold vertices were set to zero in Fiedler vector maps and 0.5 in the

422 binarized maps (so that they would not bias the calculation of averages). Figure 5A shows the thresholded

423 partitioning for the same individual shown in Figure 2. The maps used in all subsequent analyses were

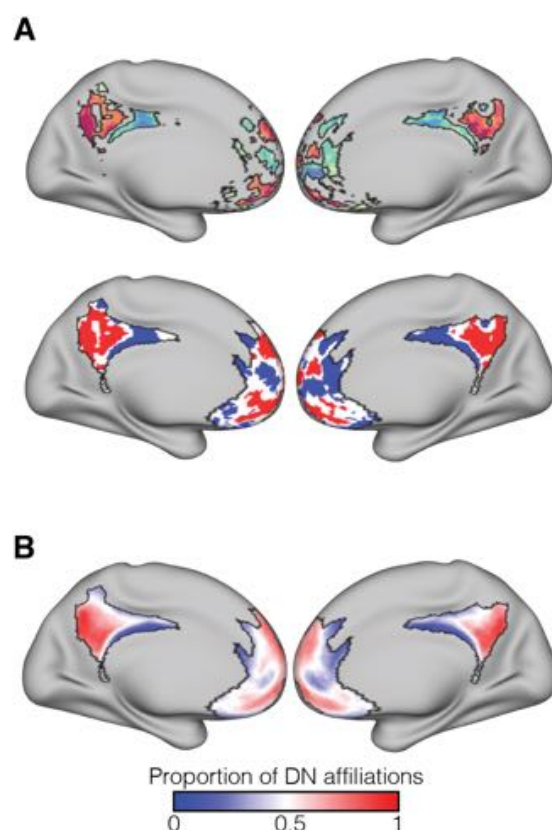424 thresholded by this individualized criterion.

20

Figure 5: Figure 5. A: Thresholded Fiedler vector map for subject 100307 (top), and its binarized form (bottom). Subthreshold values effectively formed a third community of high-variability vertices. B: Mean of the binarized maps across all participants, indicating the proportion of DN affiliations per vertex in our sample. Colors represent PCC-based labels ('DN' versus 'non-DN'), which were applied in a subsequent step following the data-driven community-detection analysis and which were necessarily well-aligned in PCC. This aggregate map shows the common organizational principle of the DN and non-DN communities, while also showing the high level of variability in mPFC.

With these thresholded partitions, we recomputed the overall similarity across participants. Compared to before, there was lower topographic agreement across individuals (mean ARI = 0.07, SD = 0.04). The same was true for both PCC (mean = 0.1, SD = 0.07) and mPFC (mean = 0.05, SD = 0.03) separately, although the significance of the differences between areas was preserved (paired permutation, $p < 0.001$; Cohen's D = 1.11). Figure 5B shows the average of the thresholded partitions across all participants, denoting the proportion of times a vertex was affiliated with the DN community. This summary illustrates the common organizational layout of both communities, but also highlights the considerable variability across individuals.

To test the possibility that the higher inter-subject variability in mPFC was driven merely by lower signal quality in the retained vertices, we quantified the temporal signal to noise ratio (tSNR) for each region, both before and after thresholding. We calculated tSNR using time series that were not demeaned, but were otherwise equivalent to the data originally used. A map of the mean tSNR across individuals can be found in Supplemental Figure 3. In terms of tSNR variability across vertices within each region, mPFC had overall greater spatial standard deviation both before and after thresholding (mPFC: pre-threshold mean spatial SD = 33.96, post-threshold mean spatial SD = 30.15; PCC: pre-threshold mean spatial SD = 15.28, post-threshold mean spatial SD = 14.59). However, mean tSNR after thresholding was significantly higher for mPFC than PCC (mPFC: mean = 77.34, SD = 13.77; PCC: mean = 64.99, SD = 10.19; permutation p-value < 0.001, Cohen's D = 1.02). This reflected a significant increase in mean tSNR in mPFC as a result of the thresholding step (pre-threshold mean = 66.5, SD = 7.87; paired permutation p-value < 0.001, Cohen's D = 0.97), whereas the mean signal quality in PCC increased only slightly (pre-threshold mean = 64.56, SD = 10.02; paired permutation p-value = 0.0384, Cohen's D = 0.04). In short, mPFC had higher overall tSNR, albeit with greater variability across nodes. Applying the thresholding step focused the analysis on vertices with high signal quality.

3.4. *Test/re-test reliability across days*

The relatively high inter-individual variability seen in the aggregate map could reflect at least three factors: (1) measurement noise, (2) dynamic variation in mPFC network organization, and (3) stable patterns of functional organization that differ across individuals. To arbitrate among these possibilities, we examined the test/re-test reliability of mPFC/PCC community structure across separate days of testing. Insofar as the observed variability reflects individual-specific brain organization, across-day ARI values should be consistently higher within-individual than between individuals (an example comparison for two individuals is provided in Supplemental Figure 2). Figure 6 shows pairwise comparisons among ten example subjects for PCC and mPFC separately (left).
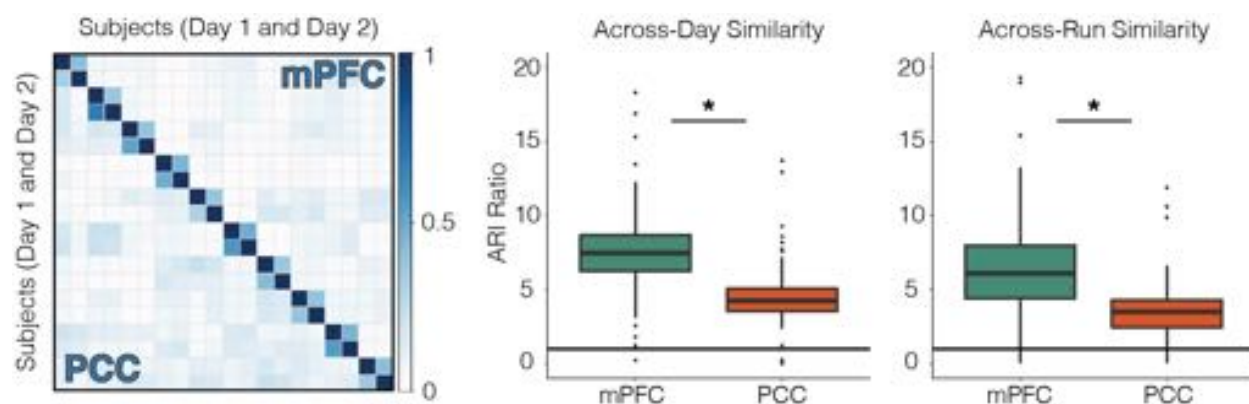
Figure 6: Figure 6. Left: Similarity matrix for 10 example participants (2 scanning days each), showing pattern agreement across days and subjects for PCC and mPFC separately. Color scale represents the ARI, which quantifies topographic similarity irrespective of how the communities are labeled. The block-diagonal structure is indicative of test-retest reliability across days within an individual. Middle: ratio of within-subject ARI to between-subject mean ARI for all individuals across days suggests idiosyncratic community arrangement for both PCC and mPFC (ratios > 1, solid line), with greater subject-specificity in mPFC. Right: within-to-between subject mean ARI ratios for run-specific partitionings again show greater subject-specific organization for mPFC.

Once again we found low alignment across individuals for PCC (mean = 0.08, SD = 0.06) and mPFC (mean = 0.03, SD = 0.03), but both areas showed comparatively high levels of within-individual agreement (PCC: mean = 0.36, SD = 0.14; mPFC: mean = 0.26, SD = 0.1). We calculated an index of relative specificity by computing the ratio of each individual's across-day (within-participant) ARI to the mean of all between-participant ARI values involving that individual. The index is expected to take on a value near 1 if partitionings are well aligned across individuals and/or are subject to a common level of measurement noise. It is expected to exceed 1 insofar as functional network organization is reliable and individual-specific. This index is intended to factor out the potential contributions of measurement noise or dynamic instability, which would introduce variability both across individuals and across days.

Figure 6 shows ARI ratios for PCC and mPFC. A signed-rank test showed evidence for specificity (i.e. ratios > 1) in both mPFC (median = 7.45, IQR = 6.08 - 8.65, V = 5037, $p < 0.001$) and PCC (median = 4.25, IQR = 3.53 - 5.29, V = 5030, $p < 0.001$). Moreover, the ratios for mPFC were significantly greater than those for PCC when compared in a paired permutation test ($p < 0.001$; Cohen's D = 0.5). This pattern was mostly unchanged when computed using modularity maximization to detect the communities, showing that the results persisted even without a forced binarization (mPFC: median = 4.46, IQR = 3.55 - 5.33;

23

471 PCC: median = 2.85, IQR = 1.94 - 3.38; difference: $p < 0.001$; Cohen's D = 0.52). These test/retest results

472 suggest that the topographic variability seen in mPFC arose at least in part from stable and subject-specific

473 organizational patterns (examples of these partitionings can be found in Supplemental Figure 4). We stress

474 that our similarity metric, the ARI, measured the similarity of partitionings in a label-agnostic manner.

475 The greater inter-individual consistency in PCC was therefore not merely an artifact of having used a PCC

476 subregion as the basis for label assignment.

477 **3.5. *Test/re-test reliability across runs***

478 We extended the analysis of per-day data by examining whether the organization of the DN could be extracted

479 using per-run data only. The duration of each run (approximately 14 min) falls well below a previously

480 suggested stability threshold for fMRI-based modularity estimations (Gordon et al., 2017). Nonetheless, high

481 ARI ratios could indicate that the SP algorithm can still obtain information about individual-specific patterns

482 of DN organization from a single run of data.

483 Run-specific SP results captured unique organizational patterns to some degree, even though the overall levels

484 of agreement decreased (PCC between subjects: mean = 0.04, SD = 0.05; mPFC between subjects: mean =

485 0.01, SD = 0.02; PCC within subjects: mean = 0.17, SD = 0.14; mPFC within subjects: mean = 0.09, SD

486 = 0.08). Supplemental Figure 4 shows that even though the community estimates were indeed less reliable

487 within-individuals than those captured using per-day data (and sometimes even failed to produce meaningful

488 partitionings), the layout of DN and non-DN was still observable in many cases, and was comparable to the

489 organization seen using larger amounts of data. We again computed each subject's ARI ratio in order to

490 quantify the specificity of the partitions, this time using the mean of 6 across-run (within-participant) ARI

491 values in the numerator of the ratio (Figure 6, right).

492 As before, a signed rank test showed that both regions had ARI ratios significantly greater than 1 (mPFC:

493 median = 6, IQR = 4.14 - 7.99, V = 4953, $p < 0.001$; PCC: median = 3.51, IQR = 2.4 - 4.26, V = 4971,

494 $p < 0.001$), and ratios for mPFC were higher than those of PCC (permutation $p = < 0.001$; Cohen's D =

495 0.94). This result further confirms that the intrinsic functional organization of mPFC is uniquely arranged

496 per individual, and provides evidence that information about such patterns can be extracted from relatively

497 small amounts of data.

3.6. *Correlation vs community detection in mPFC*

We next explored the possible advantage of community detection relative to a more conventional seed-based functional connectivity analysis for estimating the individual-specific functional topography of mPFC. We examined whether maps generated with SP were more similar per participant across days than those computed from seed-based correlations. We generated a seed time-series by averaging all vertices in the PCC region of our search space, and calculated its correlation with the activity of each vertex in mPFC. The use of the whole PCC region (instead of just 7m) was meant to represent a typical approach to seed-based connectivity that relies on the group-average location of canonical DN regions. We compared the map of correlation values in mPFC to the map of unthresholded Fiedler vector values using Spearman correlations across vertices. Pairwise spatial correlations were calculated among maps computed for each day and method from all individuals. Figure 7A shows that these pairwise comparisons resembled those from the across-day comparisons above, and suggested good alignment between methods, but particularly high agreement within subject and method.
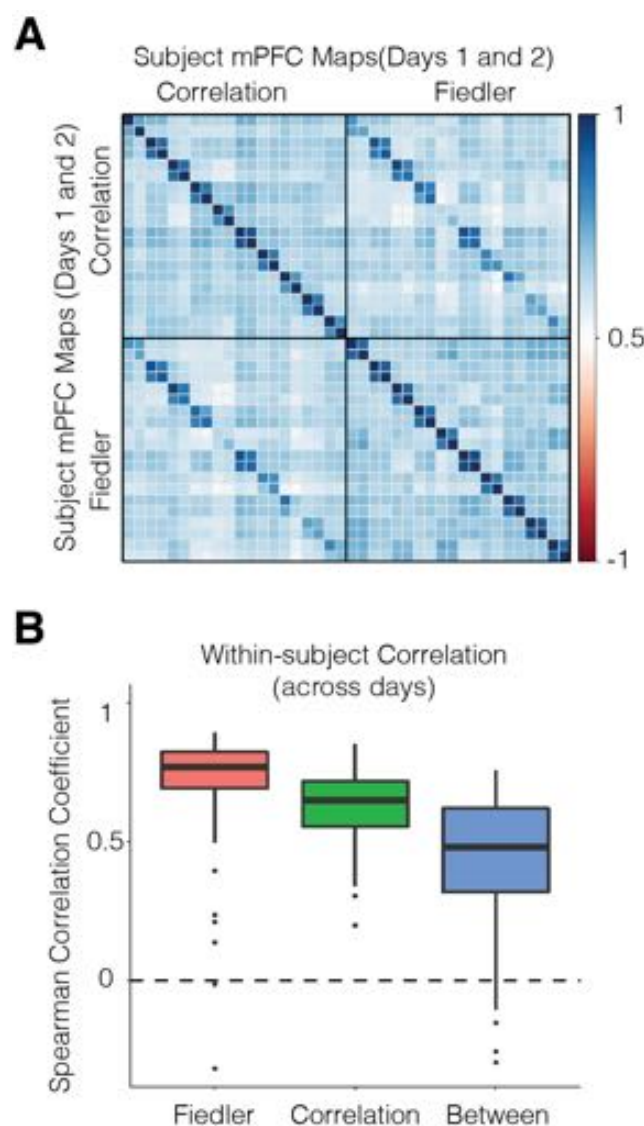
Figure 7: Figure 7. A: Correlation matrix comparing the across-day spatial stability of mPFC maps derived from seed-based functional connectivity (using a PCC seed) and the Fiedler vector for 10 example subjects. The top-left quadrant represents seed-based FC maps, and the bottom-right the Fiedler vector, with two single-day-based maps per individual. The upper-right and lower-left quadrants show across-method agreement. B: Day 1 vs Day 2 within-subject correlation coefficients for each method, as well as between methods. Community detection through spectral partitioning provided more stable estimates, even though both methods showed good levels of agreement.

510 Figure 7B shows the test/re-test reliability across days for patterns derived using community detection, seed-

511 based correlation, and across methods (e.g. Day 1 community detection versus Day 2 seed-based correlation).

512   While both approaches were reliable, community detection displayed a significantly higher median correlation

513   coefficient across days than seed-based correlation (Community: median = 0.77, SD = 0.19; Seed-based:

514   median = 0.63, SD = 0.12; paired permutation $p < 0.001$; Cohen's D = 0.54). Agreement across methods was

515   fair (median = 0.48, SD = 0.23), signifying that the two approaches identified similar topographic features but

516   also had systematic differences. These findings suggest that graph-theoretic community detection algorithms

517   are advantageous for detecting stable functional topologies, in addition to their other advantages of being

518   data-driven, unbiased and observer agnostic.

519   **3.7. *Relationship between functional organization and sulcal morphology***

520   Next, we asked if the idiosyncratic organization of the DN corresponded to patterns of sulcal morphology.

521   Several previous studies have provided evidence that sulcal and gyral organization informs the location of

522   functional effects (Amiez & Petrides, 2014; Amiez et al., 2013; Zlatkina et al., 2016). Recent work has

523   suggested that DN regions in individuals lie mostly within sulci in vmPFC (Lopez-Persem et al., 2019). We

524   sought to reproduce this relationship using the SP communities, and interrogated whether it persisted in

525   PCC and more superior mPFC regions.

526   Figure 8A shows a qualitative comparison between the thresholded DN and non-DN communities and

527   curvature maps for two individuals. In agreement with findings from Lopez-Persem and colleagues (2019), the

528   DN community appeared to overlap with the superior rostral sulcus in vmPFC in these individuals, whereas

529   the non-DN community included both gyri and sulci. A similar trend was observable in left PCC, where the

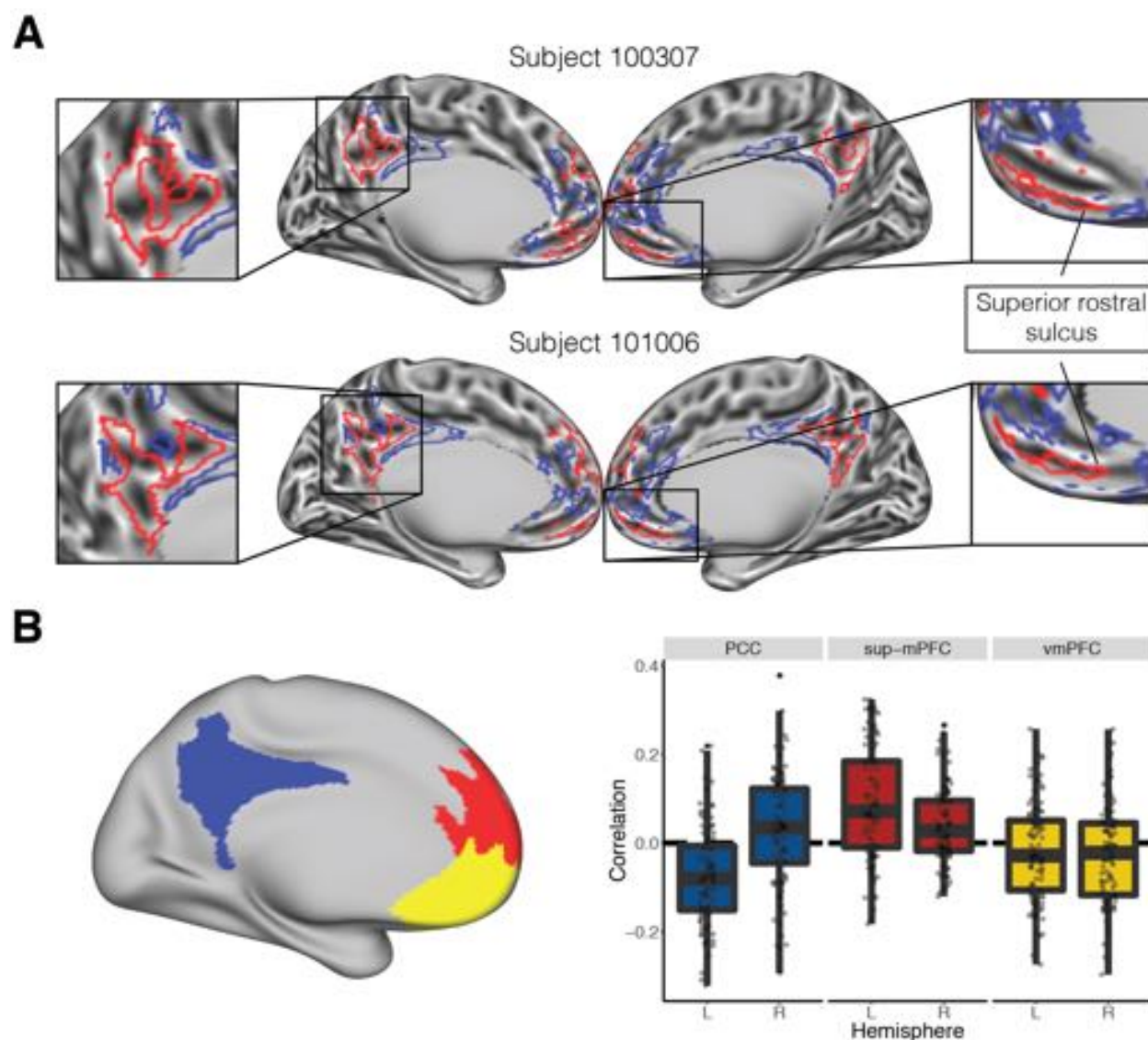530   DN community traced sulcal layouts and non-DN was more likely to appear in gyri.

27

Figure 8: Figure 8. A: Correspondence between SP communities and sulcal morphology in two example individuals. Zoomed-in boxes show areas in PCC and ventral mPFC where the DN community appears to follow sulci. The superior rostral sulcus aligned with the DN community, in agreement with findings by Lopez-Persem et al. (2019). B: Correlations between cortical curvature and the unthresholded Fiedler values. We divided the search space into three areas (left): vmPFC (yellow), superior mPFC (sup-mPFC, red), and PCC (blue). Boxplots on the right show the distribution of correlation values across individuals for each combination of region and hemisphere, indicating that the DN (defined by positive FV values) was associated with sulci in vmPFC, but with gyri within sup-dmPFC. PCC showed evidence of an opposite association across hemispheres.

531   We quantified these observations by dividing the search space into three regions: a ventral mPFC area

532   corresponding to the region tested by Lopez-Persem et al. (2019), a superior mPFC area (sup-mPFC) that

533   contained the remaining mPFC regions, and PCC (Figure 8B, left). For each individual, we correlated the

534   unthresholded Fiedler vector with cortical curvature for each combination of region and hemisphere. Negative

535   correlations in this context imply that the DN was found in sulci and non-DN in gyri. Results are shown in

536   Figure 8B. Correlations tended to be slightly negative in vmPFC, both on the left (mean correlation = -0.02,

537   SE = 0.01) and right (mean correlation = -0.02, SE = 0.01); the distribution was only significantly different

538   from zero in the right hemisphere, and weakly so (one sample t-test: t = -2.18, p = 0.031, uncorrected;

539   Cohen's D = -0.22). Correlations between FV and curvature were positive and significantly different from

540   zero in sup-mPFC, both on the left (mean correlation = 0.09, SE = 0.01; one sample t-test: t = 6.95, $p <$

541   0.001; Cohen's D = 0.69) and right (mean correlation = 0.04, SE = 0.01; one sample t-test: t = 4.49, $p <$

542   0.001; Cohen's D = 0.45). Correlations in PCC were negative and significantly different from zero in the

543   left hemisphere (mean correlation = -0.08, SE = 0.01; one sample t-test: t = -6.89, $p <$ 0.001; Cohen's D =

544   -0.69), but significantly greater than zero in the right hemisphere (mean correlation = 0.03, SE = 0.01; one

545   sample t-test: t = 2.19, p = 0.031; Cohen's D = 0.22). The difference across hemispheres was significant

546   (paired t-test: t = -7.07, $p <$ 0.001; Cohen's D = -0.88). These results provide preliminary indications that

547   the association between function and structure is heterogenous across subregions of the canonical DN.

548   **3.8. *Alignment of mPFC community structure with a proposed DN sub-network organization***

549   The thresholded partitions we identified had conceptual and topographic similarities to DN sub-networks

550   A and B proposed by Braga and Buckner (2017). We explored the relationship between the two sets

551   of sub-regions by reproducing the previously described seed-based connectivity approach in two of our

552   subjects. In previous work, Braga and Buckner (2017; Braga et al., 2019) manually selected individual

553   vertices in dorsolateral prefrontal cortex (DLPFC) that produced two spatially anticorrelated, interdigitated

554   networks with distinctive patterns in the temporo-parietal junction (TPJ), inferior parietal lobule (IPL),

555   parahippocampal cortex, mPFC, and PCC. We hypothesized that if the SP communities corresponded to one

556   or both of the previously proposed sub-networks, our partitionings should match networks A and B generated

557   by seed-based functional connectivity in these diagnostic areas. For whole-brain functional connectomes from

558   two individuals (100307 and 101006), we evaluated seeds in each diagnostic region that reproduced networks

559   A and B (correlation coefficients thresholded at 0.2), and confirmed their placement based on functional

560   connectivity patterns observed in the remaining areas. In both individuals, seeds in posterior IPL and TPJ

561   most clearly identified networks A and B, respectively. The whole-brain seed-based functional connectivity

562 maps for the two individuals are juxtaposed with the corresponding community detection results in Figure 9.

563 It is worth noting that a few distinguishing features are missing due to below-threshold correlation values

564 (e.g. network B in right PCC of 100307).

565 Visual inspection of these networks showed high similarity between our DN community and the previously

566 reported sub-network A. However, the non-DN community filled areas not covered by either DN-A or DN-B.

567 Since this three-network configuration is at odds with the two-network solution suggested in our previous

568 analyses (i.e. comparison with modularity), we ran additional evaluations to confirm its existence. First, we

569 reproduced the whole-brain k-means clustering analysis (12 clusters, 100 iterations) performed by Braga et

570 al. (2019) using the full time series for two subjects (Supplemental Figure 5A). In addition to identifying

571 DN networks A and B through this approach (in line with previous findings), we found a third cluster that

572 aligned well with the non-DN community. To understand why modularity maximization did not identify

573 the same three discrete clusters within the search space, we performed a silhouette analysis to determine

574 the ideal number of clusters in our search space (Supplemental Figure 5B). For all 100 individuals, we ran

575 k-means clusterings restricted to the mPFC/PCC search space with a specified number of clusters ranging

576 from 2 to 5, and computed a silhouette score for each solution (higher silhouette scores indicate a better fit).

577 Scores decreased as the number of clusters increased beyond 2 for all individuals, suggesting that a bisection

578 was indeed the best solution. Paired permutations comparing silhouette scores across individuals indicated

579 that the difference between two (mean = 0.042, SE = 0.001) and three (mean = 0.032, SE = 0.0009) cluster

580 solutions was significant ($p < 0.0001$, Cohen's D = 0.96). Visualization of a two-cluster k-means revealed a

581 close match with partitionings estimated through modularity, and are comparable to those produced by SP

582 prior to thresholding (Supplemental Figure 5A, bottom rows). These analyses suggest that SP isolated DN-A

583 and the non-DN community as the dominant opposite signals within our search space, but that DN-B is

584 observable once we take advantage of the continuous information contained in the Fiedler vector.

585 These results support the idea that the two approaches serve complementary purposes. Whereas Braga and

586 colleagues (2017; 2019) identified subdivisions within the DN, the present community detection approach

587 might be better understood as partitioning DN from non-DN cortex. Furthermore, the results show that

588 the continuous-valued output of our approach provides a method for estimating the location of the three

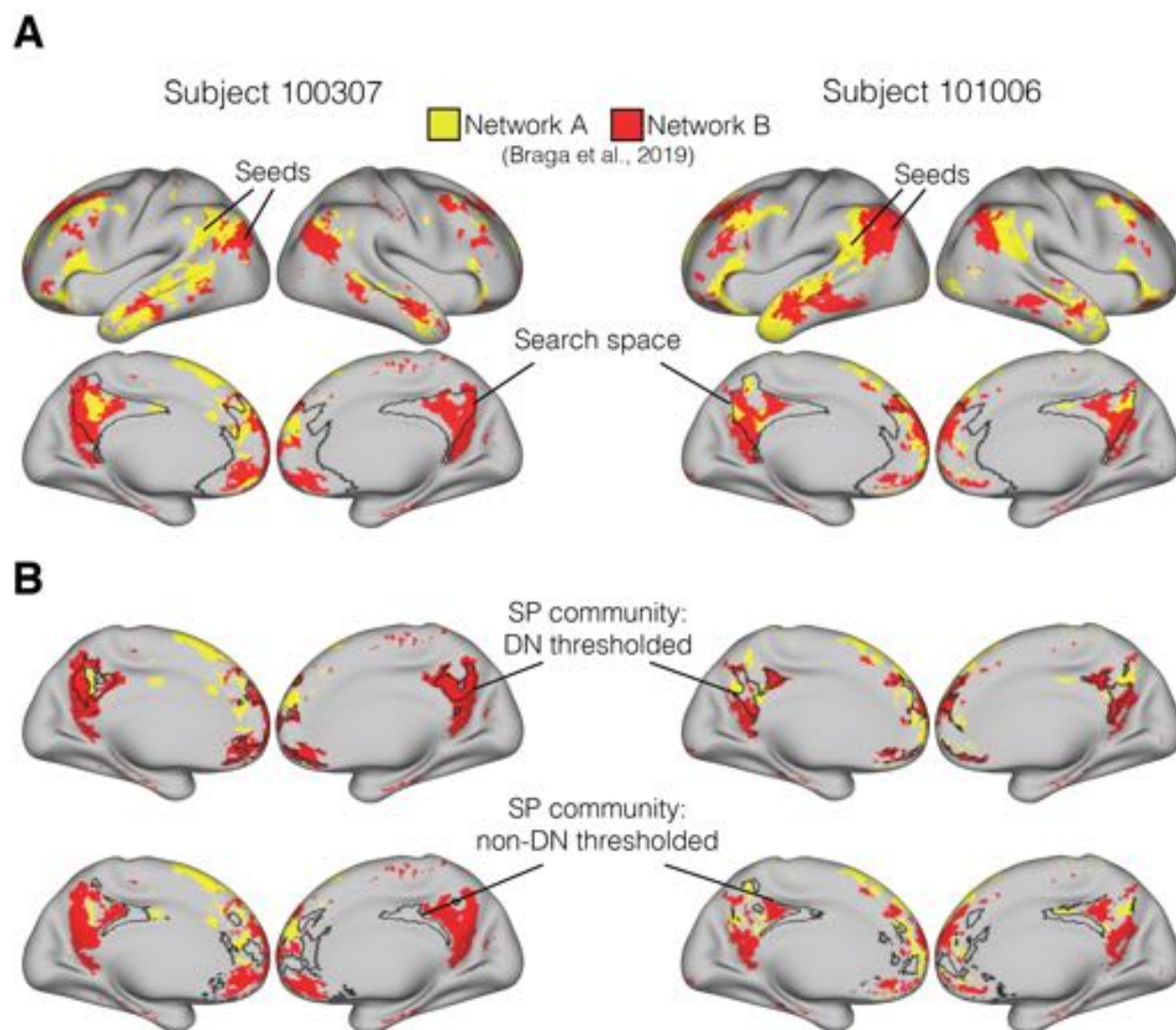589 networks in PCC and mPFC that is less computationally demanding than full-brain clustering.

Figure 9: Figure 9. Qualitative comparison between DN sub-networks A and B (estimated based on descriptions from Braga et al. (2019)) and SP communities for two individuals. Panel A: Whole-brain networks A and B produced by selecting seeds in TPJ, with our community detection search space delineated by black borders. Correlation values are thresholded at 0.2. Panel B: thresholded communities (indicated by borders) show strong resemblance between the DN community and network A. The non-DN community covers sections of cortex not associated with either DN sub-network.

4. Discussion

A considerable amount of meta-analytic work has been dedicated to characterizing the brain activity patterns associated with psychological processes in medial prefrontal cortex (mPFC), revealing both dissociable and

31

593 overlapping activation across domains (De La Vega et al., 2016; Hiser & Koenigs, 2018; Kragel et al., 2018).

594 For example, topographic patterns associated with subjective valuation and with the default network (DN)

595 have been suggested to be indistinguishable in mPFC, with overlap also partially extending to posterior

596 cingulate cortex (PCC) (Acikalin et al., 2017; Bartra et al., 2013; Clithero & Rangel, 2014; Laird et al., 2009).

597 This apparent overlap of task-related effects with DN regions has important implications, as it has motivated

598 theoretical proposals about ways in which these superficially dissimilar domains might involve a shared set of

599 core cognitive processes (Acikalin et al., 2017; Clithero & Rangel, 2014; Northoff & Hayes, 2011).

600 However, the interpretation of overlap in group-level data depends on the degree to which functional

601 organization is heterogeneous across individuals. Recent studies have shown that heteromodal brain regions

602 have considerable variability in functional connectivity across individuals (Mueller et al., 2013), individual-

603 specific functional topography can be occluded in aggregative estimations (Braga & Buckner, 2017; Gordon

604 et al., 2017; Michalka et al., 2015; Tobyne et al., 2018), and overlap in functional activation can vanish with

605 increases in spatial precision (Woo et al., 2014). These findings suggest that group-level and meta-analysis-

606 level overlap does not necessarily imply overlap in individual brains. To date, our understanding of the

607 individual-level heterogeneity in the functional topography of mPFC has been mostly descriptive (Braga &

608 Buckner, 2017; Braga et al., 2019; Gordon et al., 2017). A strong test of the overlap between task-related

609 effects and DN regions would require a method to reliably and precisely capture the functional topography of

610 mPFC in isolated individuals, as well as a quantitative estimate of the degree of topographic heterogeneity

611 across a large group of individuals.

612 Here we address these challenges by using spectral partitioning (SP), a graph-theoretic community detection

613 algorithm that efficiently separates a network into two (Fiedler, 1975; Higham et al., 2007; Toker & Sommer,

614 2019). For each of 100 individuals, we subdivided canonical DN regions into DN and non-DN communities.

615 Restricting our analyses to a general mPFC/PCC search space made it appropriate to use a technique that

616 identified a vertex-wise, binary partitioning that was sensitive to the complex topography of the brain. This

617 contrasts with whole-brain network analyses, which need to allow for multiple sub-networks and which often

618 use parcels that are several orders of magnitude larger than vertices as the units of analysis. Partitioning

619 an individual's brain network through SP has a number of advantages, including identifying communities

620 deterministically, constraining communities to contain a similar number of vertices (i.e. preventing the

621 allocation of most vertices to a single community), providing continuous values that relate to the strength of a

622 node's community affiliation, and the ability to diagnose the connectedness of a network through examination

623 of its resulting eigenvalues (Chung, 1997; Higham et al., 2007). Comparisons with partitionings formed by

624 modularity maximization, which heuristically determines the ideal number of communities (Garcia et al.,

32

625 2018), as well as a silhouette analysis, suggested the binary partitioning was appropriate.

626 We found a generalizable pattern across individual partitionings, in which the DN community covered ventral
627 and anterior/superior mPFC and posterior PCC, with the non-DN community concentrated in pregenual
628 ACC and anterior PCC. The precise spatial positioning of this general community structure was highly
629 heterogenous across individuals, yet stable across test/re-test evaluations within-individual. The idiosyncrasy
630 in functional topography was particularly pronounced in mPFC, and was identified in both run-based and
631 day-based analyses. Individual-specificity could theoretically arise from a variety of sources. For example,
632 individual variability could be due to shifts in functional organization that are independent of structural
633 features (Conroy et al., 2013; Nenning et al., 2017), or could relate to the pattern of functional connections
634 with the rest of the brain (Mars et al., 2018; Passingham et al., 2002; Tobyne et al., 2018). Alternatively, the
635 functional topography of mPFC could be governed by its underlying sulcal and gyral organization, which
636 has been shown to vary systematically across individuals (Mackey & Petrides, 2014). Our results offer some
637 support for this idea, echoing previous findings that DN is contained within sulci (in particular the superior
638 rostral sulcus) in vmPFC (Lopez-Persem et al., 2019). Structure/function associations were heterogeneous
639 in other regions; DN tended to be located in gyri in more superior mPFC regions, whereas the association
640 differed across hemispheres in PCC. Future studies should further characterize this heterogeneous relationship.
641 Another important goal for future work will be to assess whether the network layout in these regions can also
642 be predicted on the basis of other aspects of brain structure, such as myeloarchitecture (Glasser et al., 2016)
643 or structural connectivity (Osher et al., 2016; Saygin et al., 2011, 2016).

644 Network-partitioning methods such as SP are data-driven, and therefore provide no labeling information
645 about the resulting communities. We circumvented this issue by independently identifying the DN community
646 based on its coverage of area 7m, a region in PCC that was preferentially associated with the DN relative
647 to subjective valuation in our meta-analysis. We were able to apply labels derived from this group-level
648 approach on the basis of the topography in PCC, where functional organization was more consistent across
649 individuals. Because each community spanned both mPFC and PCC, the labels extended to mPFC where
650 topography was more heterogeneous.

651 Our results extend previous work that described individual-specific brain organization. Several recent
652 investigations have identified topographic heterogeneity using a different data aspect ratio than we used here
653 (a small number of individuals and a large number of scanning sessions per individual; Braga & Buckner,
654 2017; Braga et al., 2019; Gordon et al., 2017). Previous work has also shown that functional correlations
655 among pre-defined cortical parcels are highly stable within an individual (Gratton et al., 2018; Kong et al.,
656 2018). Here we were able to quantify the variability and stability of functional topography in a large sample

657 at a fine, vertex-level spatial granularity, using moderately low amounts of data (down to a single 14 minute

658 scan, although estimates based on more data were more reliable). The motivation to subdivide DN also stems

659 from recent work by Kernbach et al. (2018), which identified specialized communication of parcels within DN

660 with the rest of the brain in a large pool of individuals.

661 In addition to the technical advantages noted above, the SP algorithm offers analytical advantages specific to

662 neuroscience. We found that SP outperformed a traditional seed-based correlation approach in capturing

663 idiosyncratic functional topography. Community detection methods such as SP are stabilized by relying

664 on all pairwise correlations among cortical vertices (rather than correlations with an individual seed). In

665 addition, we found we could threshold the underlying Fiedler vector on the basis of the temporal stability of

666 SP results. The magnitude of Fiedler vector values has been recently used to characterize the continuous

667 connectivity profile of the insula with the rest of the brain, challenging the notion of discrete parcellations

668 in that region (Tian & Zalesky, 2018). The combination of discrete classification and graded information

669 yielded by SP provides additional flexibility and richness relative to some other clustering algorithms.

670 The community organization of PCC and mPFC was congruent with DN sub-networks A and B proposed

671 by Braga & Buckner (2017; Braga et al., 2019). The topography of our thresholded DN community closely

672 matched network A, whereas our non-DN community included cortical territory that was not part of either DN

673 network. Subthreshold vertices from the SP communities in turn overlapped with DN-B vertices. Our findings

674 therefore complement the initial identification of DN sub-networks by quantifying the systematic variability

675 of their underlying topography in a larger group of people. Understanding the interaction of networks DN-A,

676 DN-B, and non-DN is an important goal for future research. SP is related to methods that have gained

677 traction recently for distinguishing functional cortical gradients (Huntenburg et al., 2018; Margulies et al.,

678 2016; Tian & Zalesky, 2018). A valuable goal for future work would be to assess whether DN-A and DN-B

679 form part of a gradual information processing sequence, or if their functions can be discretized. Regardless,

680 this set of results collectively suggests that canonical DN regions can be topographically partitioned into DN

681 and non-DN communities, and that the DN community can in turn be further divided into sub-networks A

682 and B.

683 **4.1. *Conclusion***

684 Our findings show that the functional topography of mPFC is variable across a large pool of individuals,

685 and that the SP algorithm is a useful tool for identifying individualized topography in a data-driven way.

686 The ability to capture an individual's functional topography without the need for group priors is clinically

34

687 relevant, as it could help target the assessment of mPFC activity changes in disorders such as depression
688 and schizophrenia (Hiser & Koenigs, 2018). It will be beneficial for future task-based fMRI experiments
689 to be able to characterize where task-evoked activity is situated relative to an individual's overall mPFC
690 organization. Our work is relevant to interpreting the overlap of DN regions with task-related brain activity
691 in numerous cognitive domains, including valuation (Acikalin et al., 2017; Shenhav & Karmarkar, 2019),
692 memory (Euston et al., 2012), and self-referential thought (Mitchell et al., 2005). An individualized frame of
693 reference will enhance the ability of future studies to gauge similarities and differences among brain activity
694 patterns associated with diverse psychological domains.

Acknowledgements

Supplemental Materials

Table 1. Parcels from Glasser et al. (2016) contained in the search space.

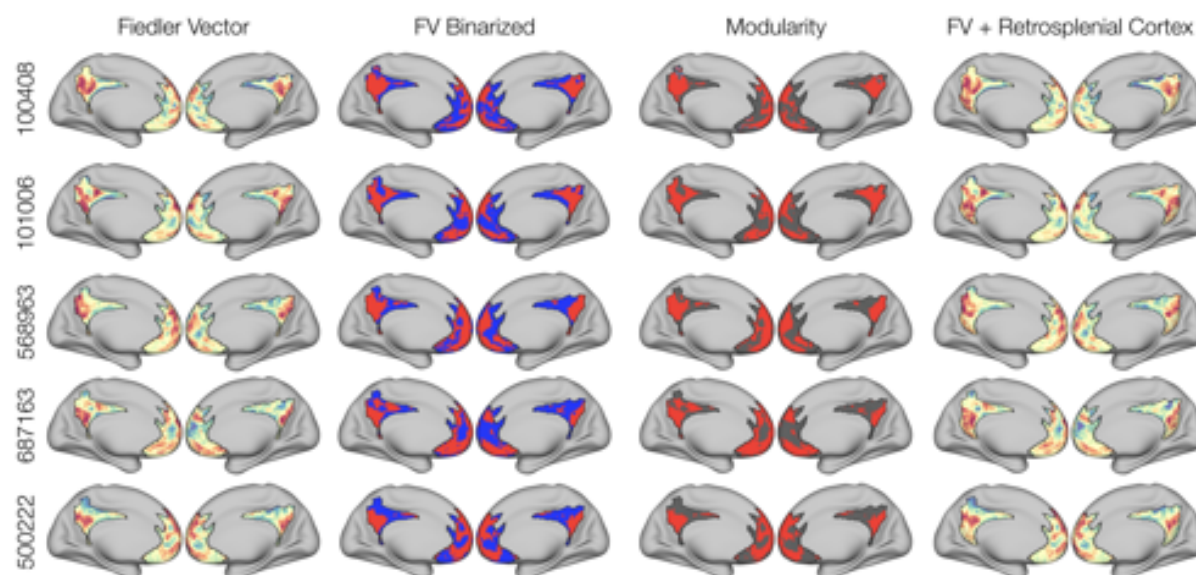| Hemisphere	mPFC	PCC
Left	10d, 10r, 10v, 25, 9m, a24, d32, OFC, p24, p32, s32	23d, 31a, 31pd, 31pv, 7m, d23ab, PCV, RSC, v23ab
Right	10d, 10r, 10v, 25, 9a, 9m, a24, d32, OFC, p24, p32, s32	23d, 31a, 31pd, 31pv, 7m, d23ab, RSC, v23ab

Figure S1: Supplemental Figure 1. Additional examples of individualized partitionings. The first two columns show both Fiedler vector values and binarized communities, respectively. A common organizational principle is visible, even though it shifts topographically across individuals. The organization is also evident when using Modularity (third column), even though some isolated vertices were sometimes placed in a small third community (see subject 100408). The fourth column shows Fiedler vector maps after adding retrosplenial cortex (a common component of canonical DN affected by task-deactivation). The addition of this area to the search space does not alter the original results, and the retrosplenial region tends to be included in the DN community.
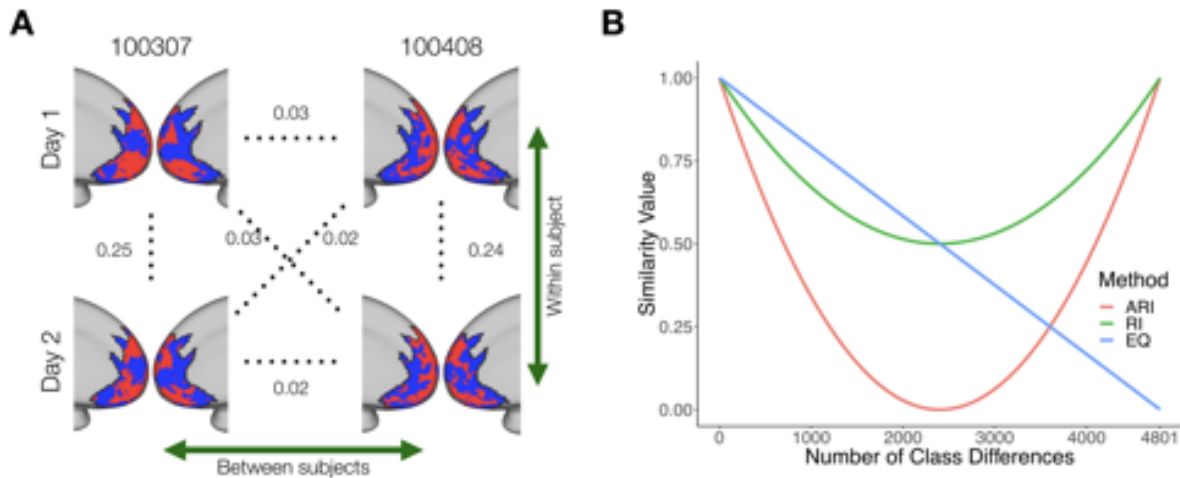
705 \begin{figure}[H]

706 {

707   }

708 \caption{Supplemental Figure 2. A: Example of an across-day comparison using ARI for two subjects (100307

709 and 100408). This reflects how qualitatively similar, within-subject partitionings can have relatively small

710 ARI values (here 0.24-0.25), and how partitionings across individuals are much closer to the chance level of

711 zero. B: Simulated comparison between two binary partitionings. The allegiance of each node is progressively

712 switched, and the agreement between the new vector and the original one is computed on each change. The

713 x-axis shows the number of nodes switched. Comparing the increasingly dissimilar maps by computing the

714 proportion of equal cluster labelings (EQ) shows the expected linear decrease in similarity. The unadjusted

715 form of the ARI (RI) displays a nonlinearly decaying similarity, and increases after reaching 50% as a result

716 of node pairs once again being grouped in the same/different clusters (making the index label-agnostic). The

717 ARI decays more steeply as a function of increasing dissimilarity, reaching 0 at chance levels. Low ARI

718 values can therefore still occur when there is systematic agreement between partitionings.} \end{figure}
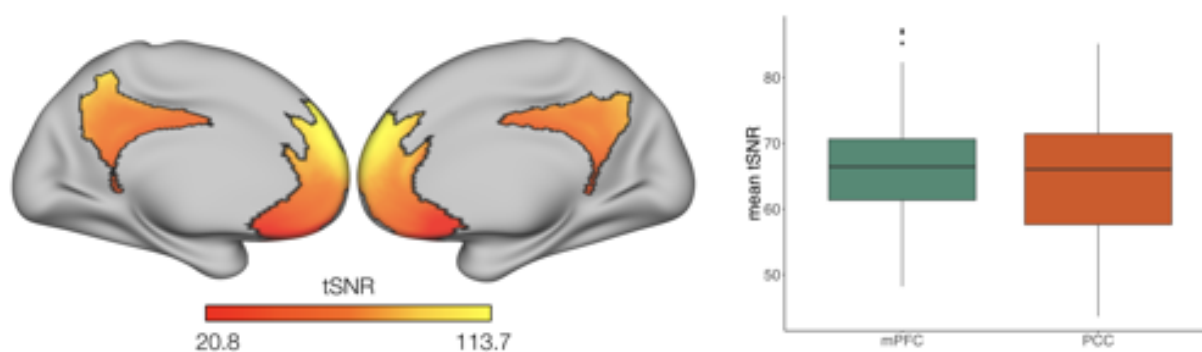
39

Figure S2: Supplemental Figure 3. BOLD signal quality in the mPFC and PCC search space. Left: Surface map displaying the vertex-wise mean tSNR across individuals. Right: Mean tSNR for mPFC and PCC across individuals.
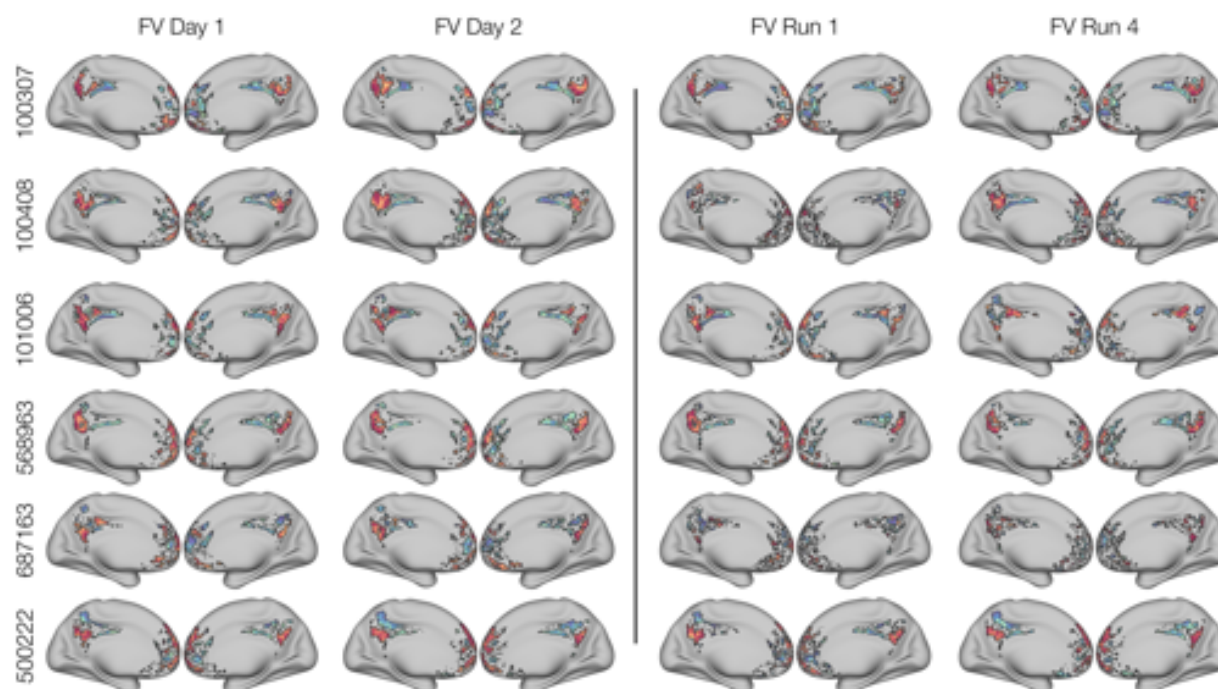
Figure S3: Supplemental Figure 4. Visual examples of idiosyncratic organization across days and runs. Left: Thresholded partitionings captured with SP were highly similar across days within individuals, but were topographically distinct across individuals. The organization estimated for each day was generally similar to that captured using the full time series (Supplemental Figure 1). Right: Thresholded partitionings estimated using the first scanning run from day 1, and the last scanning run from day 2. As expected, the considerable reduction in the amount of data used decreased the reliability of the community localization across single scanning runs, which were in some cases irrecoverable (e.g. subjects 100408 and 687163). Even so, the general location of DN and non-DN was still observable in many cases, and is comparable to the organization seen using larger amounts of data. This shows that even with notably noisier estimates and lower within-individual ARI values from working with less data, it was possible to gain information about the general location of DN and non-DN in individuals.
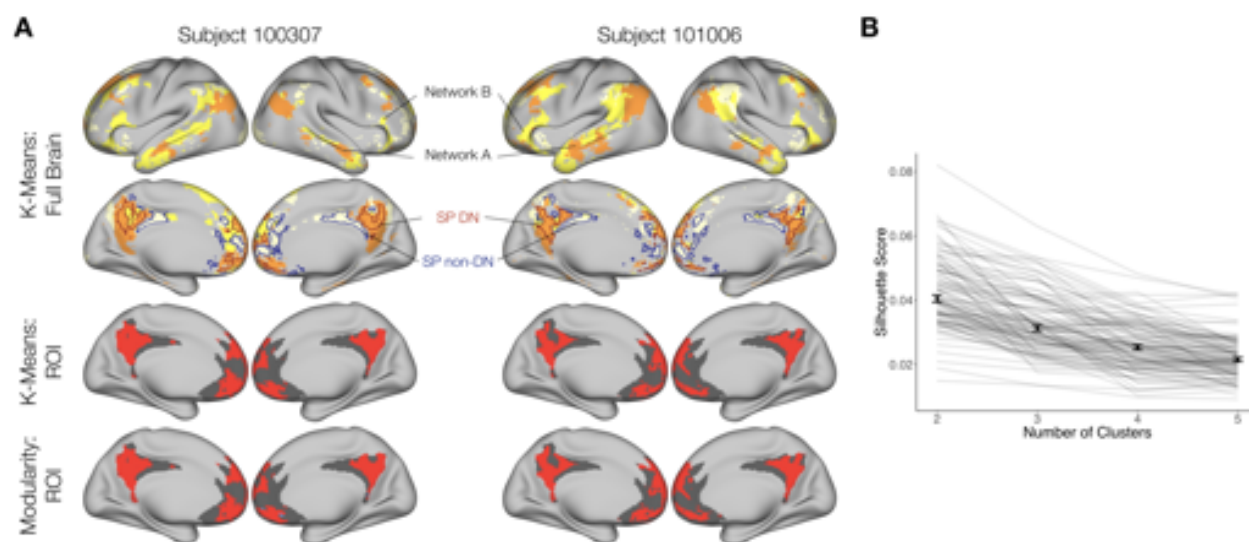
Figure S4: Supplemental Figure 5. Additional checks to confirm the match between our findings and Braga et al. (2019). A: DN sub-networks A and B identified through whole-brain k-means clustering were congruent with the existence of a third sub-network, which matched the non-DN SP community (top rows). Limiting k-means to two clusters within the search space aligned with results from modularity (bottom two rows). B: K-means based silhouette scores were computed per individual to determine the appropriate number of clusters within the search space (the higher the score, the better). This showed that two networks produced the preferred solution.

References

Acikalin, M. Y., Gorgolewski, K. J., & Poldrack, R. A. (2017). A coordinate-based meta-analysis of overlaps in regional specialization and functional connectivity across subjective value and default mode networks. *Frontiers in Neuroscience*, *11*(JAN), 1–11. https://doi.org/10.3389/fnins.2017.00001

Amiez, C., & Petrides, M. (2014). Neuroimaging evidence of the anatomo-functional organization of the human cingulate motor areas. *Cerebral Cortex*, *24*(3), 563–578. https://doi.org/10.1093/cercor/bhs329

Amiez, C., Neveu, R., Warrot, D., Petrides, M., Knoblauch, K., & Procyk, E. (2013). The location of feedback-related activity in the midcingulate cortex is predicted by local morphology. *Journal of Neuroscience*, *33*(5), 2217–2228. https://doi.org/10.1523/JNEUROSCI.2779-12.2013

Andrews-Hanna, J. R., Reidler, J. S., Huang, C., & Buckner, R. L. (2010). Evidence for the Default Network's Role in Spontaneous Cognition. *Journal of Neurophysiology*, *104*(1), 322–335. https://doi.org/10.1152/jn.00830.2009

Bartra, O., McGuire, J. T., & Kable, J. W. (2013). The valuation system: A coordinate-based meta-analysis of BOLD fMRI experiments examining neural correlates of subjective value. *NeuroImage*, *76*, 412–427. https://doi.org/10.1016/j.neuroimage.2013.02.063

Bassett, D. S., & Sporns, O. (2017). Network neuroscience. *Nature Neuroscience*, *20*(3), 353–364. https://doi.org/10.1038/nn.4502

Belkin, M., & Niyogi, P. (2003). Laplacian eigenmaps for dimensionalitu reduction and data representation. *Neural Computation*, *15*, 1373–1396. https://doi.org/10.1162/089976603321780317

Braga, R. M., & Buckner, R. L. (2017). Parallel Interdigitated Distributed Networks within the Individual Estimated by Intrinsic Functional Connectivity. *Neuron*, *95*(2), 457–471.e5. https://doi.org/10.1016/j.neuron.2017.06.038

Braga, R. M., Van Dijk, K. R., Polimeni, J. R., Eldaief, M. C., & Buckner, R. L. (2019). Parallel distributed networks resolved at high resolution reveal close juxtaposition of distinct regions. *Journal of Neurophysiology*, jn.00808.2018. https://doi.org/10.1152/jn.00808.2018

Buckner, R. L., & Carroll, D. C. (2007). Self-projection and the brain. *Trends in Cognitive Sciences*, *11*(2), 49–57. https://doi.org/10.1016/j.tics.2006.11.004

Buckner, R. L., & DiNicola, L. M. (2019). The Brain's Default Network: Updated Anatomy, Physiology, and

43

Evolving Insights. *Nature Reviews Neuroscience*. https://doi.org/10.1038/s41583-019-0212-7

Buckner, R. L., Andrews-Hanna, J. R., & Schacter, D. L. (2008). The brain's default network: Anatomy, function, and relevance to disease. *Annals of the New York Academy of Sciences*, *1124*, 1–38. https://doi.org/10.1196/annals.1440.011

Burgess, G. C., Kandala, S., Nolan, D., Laumann, T. O., Power, J. D., Adeyemo, B., . . . & Barch, D. M. (2016). Evaluation of Denoising Strategies to Address Motion-Correlated Artifacts in Resting-State Functional Magnetic Resonance Imaging Data from the Human Connectome Project. *Brain Connectivity*, *6*(9), 669–680.

Chung, F. R. K. (1997). *Spectral Graph Theory* (Vol. 92). American Mathematical Soc.

Clauset, A., Newman, M. E. J., & Moore, C. (2004). *Finding community structure in very large networks*. *066111*, 1–6. https://doi.org/10.1103/PhysRevE.70.066111

Clithero, J. A., & Rangel, A. (2014). Informatic parcellation of the network involved in the computation of subjective value. *Social Cognitive and Affective Neuroscience*, *9*(9), 1289–1302. https://doi.org/10.1093/scan/nst106

Conroy, B. R., Singer, B. D., Guntupalli, J. S., Ramadge, P. J., & Haxby, J. V. (2013). Inter-subject alignment of human cortical anatomy using functional connectivity. *NeuroImage*, *81*, 400–411. https://doi.org/10.1016/j.neuroimage.2013.05.009

Csardi, G., & Nepusz, T. (2006). The igraph software package for complex network research. *InterJournal Complex Systems*, *1695*.

Dale, A. M., Fischl, B., & Sereno, M. I. (1999). Cortical surface-based analysis: I. Segmentation and surface reconstruction. *NeuroImage*, *9*(2), 179–194. https://doi.org/10.1006/nimg.1998.0395

De La Vega, A., Chang, L. J., Banich, M. T., Wager, T. D., & Yarkoni, T. (2016). Large-Scale Meta-Analysis of Human Medial Frontal Cortex Reveals Tripartite Functional Organization. *The Journal of Neuroscience*, *36*(24), 6553–6562. https://doi.org/10.1523/JNEUROSCI.4402-15.2016

DiNicola, L. M., Braga, R. M., & Buckner, R. L. (2019). Parallel Distributed Networks Dissociate Episodic and Social Functions Within the Individual. *BioRxiv*. https://doi.org/https://doi.org/10.1101/733048

Euston, D. R., Gruber, A. J., & McNaughton, B. L. (2012). The role of medial prefrontal cortex in memory and decision making. *Neuron*, *76*(6), 1057–1070. https://doi.org/10.1016/j.neuron.2012.12.002

Fedorenko, E., Duncan, J., & Kanwisher, N. (2012). Language-selective and domain-general regions lie side

44

776   by side within Broca's area. *Current Biology*, *22*(21), 2059–2062. https://doi.org/10.1016/j.cub.2012.09.011

777   Fiedler, M. (1975). A Property of Eigenvectors of Nonnegative Symmetric Matrices and its Application to

778   Graph Theory. *Czechoslovak Mathematical Journal*, *25*(100), 619–633.

779   Fischl, B., Sereno, M. I., & Dale, A. M. (1999). Cortical surface-based analysis: II. Inflation, flattening, and

780   a surface-based coordinate system. *NeuroImage*, *9*(2), 195–207. https://doi.org/10.1006/nimg.1998.0396

781   Fortunato, S., & Hric, D. (2016). Community detection in networks: A user guide. *Physics Reports*, *659*,

782   1–44. https://doi.org/10.1016/j.physrep.2016.09.002

783   Fox, M. D., Snyder, A. Z., Vincent, J. L., Corbetta, M., Van Essen, D. C., & Raichle, M. E. (2005). The

784   human brain is intrinsically organized into dynamic, anticorrelated functional networks. *Proceedings of the*

785   *National Academy of Sciences*, *102*(27), 9673–9678. https://doi.org/10.1073/pnas.0504136102

786   Fritsch, A. (2012). *mcclust: Process an MCMC Sample of Clusterings. R package version 1.0.* Retrieved

787   from https://cran.r-project.org/package=mcclust

788   Garcia, J. O., Ashourvan, A., Muldoon, S., Vettel, J. M., & Bassett, D. S. (2018). Applications of

789   Community Detection Techniques to Brain Graphs: Algorithmic Considerations and Implications for Neural

790   Function. *Proceedings of the IEEE*, *106*(5), 846–867. https://doi.org/10.1109/JPROC.2017.2786710

791   Ghasemian, A., Hosseinmardi, H., & Clauset, A. (2019). Evaluating Overfit and Underfit in Models of

792   Network Community Structure. *IEEE Transactions on Knowledge and Data Engineering*.

793   https://doi.org/10.1109/TKDE.2019.2911585

794   Gkantsidis, C., Mihail, M., & Zegura, E. (2003). Spectral analysis of Internet topologies. *Proc. IEEE*

795   *INFOCOM*, *00*(C), 364–374. https://doi.org/10.1109/INFCOM.2003.1208688

796   Glasser, M. F., Coalson, T. S., Robinson, E. C., Hacker, C. D., Harwell, J., Yacoub, E., . . . Van Essen, D. C.

797   (2016). A multi-modal parcellation of human cerebral cortex. *Nature*, *536*(7615), 171–178.

798   https://doi.org/10.1038/nature18933

799   Glasser, M. F., Sotiropoulos, S. N., Wilson, J. A., Coalson, T. S., Fischl, B., Andersson, J. L., . . . Jenkinson,

800   M. (2013). The minimal preprocessing pipelines for the Human Connectome Project. *NeuroImage*, *80*,

801   105–124. https://doi.org/10.1016/j.neuroimage.2013.04.127

802   Gordon, E. M., Laumann, T. O., Gilmore, A. W., Newbold, D. J., Greene, D. J., Berg, J. J., . . . Dosenbach,

803   N. U. (2017). Precision Functional Mapping of Individual Human Brains. *Neuron*, *95*(4), 791–807.e7.

804   https://doi.org/10.1016/j.neuron.2017.07.011

805   Gratton, C., Laumann, T. O., Nielsen, A. N., Greene, D. J., Gordon, E. M., Gilmore, A. W., . . . Petersen, S.

806   E. (2018). Functional Brain Networks Are Dominated by Stable Group and Individual Factors, Not

807   Cognitive or Daily Variation. *Neuron*, 439–452. https://doi.org/10.1016/j.neuron.2018.03.035

808   Greicius, M. D., Krasnow, B., Reiss, A. L., & Menon, V. (2003). *Functional connectivity in the resting brain:*

809   *A network analysis of the default mode hypothesis. 100* (1), 253–258.

810   https://doi.org/10.1073/pnas.0135058100

811   Griffanti, L., Salimi-Khorshidi, G., Beckmann, C. F., Auerbach, E. J., Douaud, G., Sexton, C. E., . . . Smith,

812   S. M. (2014). ICA-based artefact removal and accelerated fMRI acquisition for improved resting state

813   network imaging. *NeuroImage*, *95*, 232–247. https://doi.org/10.1016/j.neuroimage.2014.03.034

814   Guntupalli, J. S., Feilong, M., & Haxby, J. V. (2018). A computational model of shared fine-scale structure

815   in the human connectome. *PLoS Computational Biology*, *14* (4), 1–26.

816   https://doi.org/10.1371/journal.pcbi.1006120

817   Gusnard, D. A., Akbudak, E., Shulman, G. L., & Raichle, M. E. (2001). Medial prefrontal cortex and

818   self-referential mental activity: Relation to a default mode of brain function. *Proceedings of the National*

819   *Academy of Sciences*, *98* (7), 4259–4264. https://doi.org/10.1073/pnas.071043098

820   Hassabis, D., & Maguire, E. A. (2007). Deconstructing episodic memory with construction. *Trends in*

821   *Cognitive Sciences*, *11* (7), 299–306. https://doi.org/10.1016/j.tics.2007.05.001

822   Higham, D. J., Kalna, G., & Kibble, M. (2007). Spectral clustering and its use in bioinformatics. *Journal of*

823   *Computational and Applied Mathematics*, *204* (1), 25–37. https://doi.org/10.1016/j.cam.2006.04.026

824   Hiser, J., & Koenigs, M. (2018). The Multifaceted Role of the Ventromedial Prefrontal Cortex in Emotion,

825   Decision Making, Social Cognition, and Psychopathology. *Biological Psychiatry*, *83* (8), 638–647.

826   https://doi.org/10.1016/j.biopsych.2017.10.030

827   Hubert, L., & Arabie, P. (1985). Comparing partitions. *Journal of Classification*, *2* (1), 193–218.

828   https://doi.org/10.1007/BF01908075

829   Huntenburg, J. M., Bazin, P. L., & Margulies, D. S. (2018). Large-Scale Gradients in Human Cortical

830   Organization. *Trends in Cognitive Sciences*, *22* (1), 21–31. https://doi.org/10.1016/j.tics.2017.11.002

831   Kable, J. W., & Glimcher, P. W. (2007). The neural correlates of subjective value during intertemporal

832   choice. *Nature Neuroscience*, *10*(12), 1625–1633.

833   Kernbach, J. M., Yeo, B. T. T., Smallwood, J., Margulies, D. S., Thiebaut de Schotten, M., Walter, H., . . .

834   Bzdok, D. (2018). Subspecialization within default mode nodes characterized in 10,000 UK Biobank

835   participants. *Proceedings of the National Academy of Sciences*, (November), 201804876.

836   https://doi.org/10.1073/pnas.1804876115

837   Kong, R., Li, J., Orban, C., Sabuncu, M. R., Liu, H., Schaefer, A., . . . Yeo, B. T. T. (2018). Spatial

838 Topography of Individual-Specific Cortical Networks Predicts Human Cognition, Personality, and Emotion.

839   *Cerebral Cortex*, (May 2018), 2533–2551. https://doi.org/10.1093/cercor/bhy123

840   Kragel, P. A., Kano, M., Van Oudenhove, L., Ly, H. G., Dupont, P., Rubio, A., . . . Wager, T. D. (2018).

841   Generalizable representations of pain, cognitive control, and negative emotion in medial frontal cortex.

842   *Nature Neuroscience*, 1. https://doi.org/10.1038/s41593-017-0051-7

843   Laird, A. R., Eickhoff, S. B., Li, K., Robin, D. A., Glahn, D. C., & Fox, P. T. (2009). Investigating the

844 Functional Heterogeneity of the Default Mode Network Using Coordinate-Based Meta-Analytic Modeling.

845   *Journal of Neuroscience*, *29*(46), 14496–14505. https://doi.org/10.1523/JNEUROSCI.4004-09.2009

846 Laumann, T. O., Gordon, E. M., Adeyemo, B., Snyder, A. Z., Joo, S. J., Chen, M. Y., . . . Petersen, S. E.

847 (2015). Functional System and Areal Organization of a Highly Sampled Individual Human Brain. *Neuron*,

848   *87*(3), 658–671. https://doi.org/10.1016/j.neuron.2015.06.037

849   Levy, I., Lazzaro, S. C., Rutledge, R. B., & Glimcher, P. W. (2011). Choice from Non-Choice: Predicting

850 Consumer Preferences from Blood Oxygenation Level-Dependent Signals Obtained during Passive Viewing.

851   *Journal of Neuroscience*, *31*(1), 118–125. https://doi.org/10.1523/JNEUROSCI.3214-10.2011

852   Lopez-Persem, A., Verhagen, L., Amiez, C., Petrides, M., & Sallet, J. (2019). The human ventromedial

853   prefrontal cortex: sulcal morphology and its influence on functional organization. *The Journal of*

854   *Neuroscience*, *39*(19), 2060–2018. https://doi.org/10.1523/JNEUROSCI.2060-18.2019

855   Mackey, S., & Petrides, M. (2014). Architecture and morphology of the human ventromedial prefrontal

856   cortex. *European Journal of Neuroscience*, *40*(5), 2777–2796. https://doi.org/10.1111/ejn.12654

857 Margulies, D. S., Ghosh, S. S., Goulas, A., Falkiewicz, M., Huntenburg, J. M., Langs, G., . . . Smallwood, J.

858 (2016). Situating the default-mode network along a principal gradient of macroscale cortical organization.

859   *Proceedings of the National Academy of Sciences*, *113*(44), 12574–12579.

860   https://doi.org/10.1073/pnas.1608282113

861 Mars, R. B., Passingham, R. E., & Jbabdi, S. (2018). Connectivity Fingerprints: From Areal Descriptions to

47

862   Abstract Spaces. *Trends in Cognitive Sciences*, *22*(11), 1026–1037. https://doi.org/10.1016/j.tics.2018.08.009

863   McKiernan, K. A., Kaufman, J. N., Kucera-Thompson, J., & Binder, J. R. (2003). A Parametric

864   Manipulation of Factors Affecting Task-induced Deactivation in Functional Neuroimaging. *Journal of*

865   *Cognitive Neuroscience*, *15*, 394–408. https://doi.org/10.1162/089892903321593117

866   Michalka, S. W., Kong, L., Rosen, M. L., Shinn-Cunningham, B. G., & Somers, D. C. (2015). Short-Term

867   Memory for Space and Time Flexibly Recruit Complementary Sensory-Biased Frontal Lobe Attention

868   Networks. *Neuron*, *87*(4), 882–892. https://doi.org/10.1016/j.neuron.2015.07.028

869   Mitchell, J. P., Banaji, M. R., & Macrae, C. N. (2005). The link between social cognition and self-referential

870   thought in the medial prefrontal cortex. *Journal of Cognitive Neuroscience*, *17*(8), 1306–1315.

871   Mueller, S., Wang, D., Fox, M. D., Yeo, B. T. T., Sepulcre, J., Sabuncu, M. R., . . . Liu, H. (2013).

872   Individual Variability in Functional Connectivity Architecture of the Human Brain. *Neuron*, *77*(3), 586–595.

873   https://doi.org/10.1016/j.neuron.2012.12.028

874   Nenning, K. H., Liu, H., Ghosh, S. S., Sabuncu, M. R., Schwartz, E., & Langs, G. (2017). Diffeomorphic

875   functional brain surface alignment: Functional demons. *NeuroImage*, *156*(December 2016), 456–465.

876   https://doi.org/10.1016/j.neuroimage.2017.04.028

877   Northoff, G., & Hayes, D. J. (2011). Is our self nothing but reward? *Biological Psychiatry*, *69*, 1019–1025.

878   https://doi.org/10.1016/j.biopsych.2010.12.014

879   Osher, D. E., Saxe, R. R., Koldewyn, K., Gabrieli, J. D., Kanwisher, N., & Saygin, Z. M. (2016). Structural

880   Connectivity Fingerprints Predict Cortical Selectivity for Multiple Visual Categories across Cortex. *Cerebral*

881   *Cortex*, *26*(4), 1668–1683. https://doi.org/10.1093/cercor/bhu303

882   Passingham, R. E., Stephan, K. E., & Kötter, R. (2002). The anatomical basis of functional localization in

883   the cortex. *Nature Reviews Neuroscience*, *3*(8), 606–616. https://doi.org/10.1038/nrn893

884   Power, J. D., Mitra, A., Laumann, T. O., Snyder, A. Z., Schlaggar, B. L., & Petersen, S. E. (2014). Methods

885   to detect, characterize, and remove motion artifact in resting state fMRI. *NeuroImage*, *84*, 320–341.

886   https://doi.org/10.1016/j.neuroimage.2013.08.048

887   R Core Computing Team. (2017). *R: A Language and Environment for Statistical Computing*. Retrieved

888   from https://www.r-project.org/

889   Reddan, M. C., Wager, T. D., & Schiller, D. (2018). Attenuating Neural Threat Expression with

890   Imagination. *Neuron*, *100*(4), 994–1005.e4. https://doi.org/10.1016/j.neuron.2018.10.047

891   Rubinov, M., & Sporns, O. (2010). Complex network measures of brain connectivity: Uses and

892   interpretations. *NeuroImage*, *52*(3), 1059–1069. https://doi.org/10.1016/j.neuroimage.2009.10.003

893   Salimi-Khorshidi, G., Douaud, G., Beckmann, C. F., Glasser, M. F., Griffanti, L., & Smith, S. M. (2014).

894   Automatic denoising of functional MRI data: Combining independent component analysis and hierarchical

895   fusion of classifiers. *NeuroImage*, *90*, 449–468. https://doi.org/10.1016/j.neuroimage.2013.11.046

896   Saygin, Z. M., Osher, D. E., Koldewyn, K., Reynolds, G., Gabrieli, J. D., & Saxe, R. R. (2011). Anatomical

897   connectivity patterns predict face selectivity in the fusiform gyrus. *Nature Neuroscience*, *15*(2), 321–327.

898   https://doi.org/10.1038/nn.3001

899   Saygin, Z. M., Osher, D. E., Norton, E. S., Youssoufian, D. A., Beach, S. D., Feather, J., . . . Kanwisher, N.

900   (2016). Connectivity precedes function in the development of the visual word form area. *Nature*

901   *Neuroscience*, *19*(9), 1250–1255. https://doi.org/10.1038/nn.4354

902   Schacter, D. L., Addis, D. R., & Buckner, R. L. (2007). Remembering the past to imagine the future: The

903   prospective brain. *Nature Reviews Neuroscience*, *8*(9), 657–661. https://doi.org/10.1038/nrn2213

904   Schiller, D., Levy, I., Niv, Y., LeDoux, J. E., & Phelps, E. A. (2008). From fear to safety and back: Reversal

905   of fear in the human brain. *Journal of Neuroscience*, *28*(45), 11517–11525.

906   https://doi.org/10.1523/JNEUROSCI.2265-08.2008

907   Shenhav, A., & Karmarkar, U. R. (2019). Dissociable components of the reward circuit are involved in

908   appraisal versus choice. *Scientific Reports*, *9*(1), 172320. https://doi.org/10.1038/s41598-019-38927-7

909   Smith, S. M., Fox, P. T., Miller, K. L., Glahn, D. C., Fox, P. M., Mackay, C. E., . . . Beckmann, C. F. (2009).

910   Correspondence of the brain's functional architecture during activation and rest. *Proceedings of the National*

911   *Academy of Sciences*, *106*(31), 13040 LP–13045. https://doi.org/10.1073/pnas.0905267106

912   Spreng, N. (2012). The fallacy of a "task-negative" network. *Frontiers in Psychology*, *3*(MAY), 1–5.

913   https://doi.org/10.3389/fpsyg.2012.00145

914   Tian, Y., & Zalesky, A. (2018). Characterizing the functional connectivity diversity of the insula cortex:

915   Subregions, diversity curves and behavior. *NeuroImage*, *183*, 716–733.

916   https://doi.org/10.1016/j.neuroimage.2018.08.055

917   Tobyne, S. M., Osher, D. E., Michalka, S. W., & Somers, D. C. (2017). Sensory-biased attention networks in

918   human lateral frontal cortex revealed by intrinsic functional connectivity. *NeuroImage*, *162*(August),

919   362–372. https://doi.org/10.1016/j.neuroimage.2017.08.020

920 Tobyne, S. M., Somers, D. C., Brissenden, J. A., Michalka, S. W., Noyce, A. L., & Osher, D. E. (2018).

921 Prediction of individualized task activation in sensory modality-selective frontal cortex with 'connectome

922 fingerprinting'. *NeuroImage*, *183*(August), 173–185. https://doi.org/10.1016/j.neuroimage.2018.08.007

923 Toker, D., & Sommer, F. T. (2019). Information Integration In Large Brain Networks. *PLoS Computational*

924   *Biology*, *15*(2). https://doi.org/10.1371/journal.pcbi.1006807

925 Van Essen, D. C., Ugurbil, K., Auerbach, E., Barch, D., Behrens, T. E., Bucholz, R., . . . Yacoub, E. (2012).

926   The Human Connectome Project: A data acquisition perspective. *NeuroImage*, *62*(4), 2222–2231.

927   https://doi.org/10.1016/j.neuroimage.2012.02.018

928 Wager, T. D., Lindquist, M. A., Nichols, T. E., Kober, H., & Van Snellenberg, J. X. (2009). Evaluating the

929 consistency and specificity of neuroimaging data using meta-analysis. *NeuroImage*, *45*(1 Suppl), S210–S221.

930   https://doi.org/10.1016/j.neuroimage.2008.10.061

931 Wang, D., Buckner, R. L., Fox, M. D., Holt, D. J., Holmes, A. J., Stoecklein, S., . . . Liu, H. (2015).

932   Parcellating cortical functional networks in individuals. *Nature Neuroscience*, *18*(12), 1853–1860.

933   https://doi.org/10.1038/nn.4164

934 Woo, C.-W., Koban, L., Kross, E., Lindquist, M. A., Banich, M. T., Ruzic, L., . . . Wager, T. D. (2014).

935 Separate neural representations for physical pain and social rejection. *Nature Communications*, *5*(May),

936   1–12. https://doi.org/10.1038/ncomms6380

937 Yeo, B. T. T., Krienen, F. M., Sepulcre, J., Sabuncu, M. R., Lashkari, D., Hollinshead, M., . . . Buckner, R.

938 L. (2011). The organization of the human cerebral cortex estimated by intrinsic functional connectivity.

939   *Journal of Neurophysiology*, *106*, 1125–1165. https://doi.org/10.1152/jn.00338.2011

940 Zilles, K., Palomero-Gallagher, N., & Amunts, K. (2013). Development of cortical folding during evolution

941   and ontogeny. *Trends in Neurosciences*, *36*(5), 275–284. https://doi.org/10.1016/j.tins.2013.01.006

942   Zlatkina, V., Amiez, C., & Petrides, M. (2016). The postcentral sulcal complex and the transverse

943   postcentral sulcus and their relation to sensorimotor functional organization. *European Journal of*

944   *Neuroscience*, *43*(10), 1268–1283. https://doi.org/10.1111/ejn.13049